

GEORGE S. DULIKRAVICH

ADVANCES IN
NUMERICAL HEAT TRANSFER

Volume 1

Edited By

W.J. Minkowycz

*Professor of Mechanical Engineering
University of Illinois
Chicago, Illinois*

E.M. Sparrow

*Professor of Mechanical Engineering
University of Minnesota
Minneapolis, Minnesota*


Taylor & Francis
Publishers since 1798

CHAPTER TEN

INVERSE SHAPE AND BOUNDARY CONDITION PROBLEMS AND OPTIMIZATION IN HEAT CONDUCTION

G.S. Dulikravich
T.J. Martin

1 INTRODUCTION

A heat conduction problem is fully defined (well-posed) by the following: the governing partial differential equation (elliptic for steady heat conduction and parabolic or hyperbolic for unsteady heat conduction), the thermal properties of the material (that is, the coefficients in the governing equation), the initial conditions and the boundary conditions (either of Dirichlet, Neumann or Robin type), the shape and size of the domain, and the internal heat source distribution. If any part of this information is unavailable, the problem is under-specified or ill-posed (inverse) [1]. This can happen in a number of practical situations.

For example, it is often difficult and even impossible to use sensors to measure temperatures and heat fluxes on certain boundaries such as those of combustion chambers. The placement of thermal sensors may also be impossible because of the prohibitively small size of the domain, as is the case of a computer chip or in the coolant flow passage of a turbine blade. Thus, in many cases, we are forced to solve an ill-posed boundary condition problem where the size and the shape of the domain are known, while thermal boundary conditions are unavailable on parts of the boundary and overspecified on the rest of the boundary [2–6].

A similar type of problem arises when thermal sensors cannot be used to evaluate heat sources in the domain because of the highly volatile environment as in the case of a buried toxic waste site. Thus, when the heat source distribution is partially or entirely unknown, we have to be given both temperature and heat flux data on at least a part of the boundary in order to solve this ill-posed (inverse) heat source problem [7–9].

Another class of inverse problems arises when the size and shape of some parts of the domain are unknown. In order to determine the remaining boundaries of the domain, we must know additional boundary conditions in the form of independently specified Dirichlet and Neumann boundary conditions at the same points of the known boundary. Thus, when the thermal boundary conditions are

overspecified on a part of the boundary and the remaining boundary is not known, the problem is referred to as an ill-posed (inverse) shape design problem [10–26].

The unsteady inverse heat conduction problems (UIHCP) represent a subclass of ill-posed problems which have been extensively investigated [27–31]. The UIHCP involves an estimation of the initial conditions (temperatures and heat fluxes) or an estimation of unsteady boundary conditions [27–36] (temperatures and heat fluxes) utilizing measured interior temperature histories. The major concern when attempting to solve the UIHCP computationally has been with the automatic filtering of noisy data in the discrete thermocouple measurements. The measurement data errors, as well as round-off errors, are amplified by the typical UIHCP algorithms. A review of the UIHCP literature reveals that the majority of researchers use the approach where the sum of squares of the error between the computed and measured temperatures is minimized with respect to the heat flux components. Among others, the method of regularizers [37], discrete mollification [38] against a suitable averaging kernel, and other filtering techniques [39] are usually implemented in order to smooth the extrapolated heat fluxes.

Methods for the solution of ill-posed (inverse) problems are common to a variety of engineering disciplines [40–42] and are regularly presented in the technical journals entitled *Inverse Problems* and *Inverse Problems in Engineering*. We will describe strictly our own efforts in developing fast and reliable algorithms for the solution of various inverse problems arising in heat conduction using either special non-iterative algorithms or iterative algorithms that make use of numerical optimization as a tool of achieving solutions of *de facto* inverse problems.

2 THEORETICAL FORMULATION

2.1 Steady State Heat Conduction

The governing heat conduction equation for the steady-state temperature distribution, $T(\mathbf{x})$, in a solid isotropic domain Ω bounded by the boundary Γ is given by

$$\nabla \cdot [k(T) \nabla T(\mathbf{x})] + L(\mathbf{x}) = 0 \quad (1)$$

Here, $k(T)$ is the temperature-dependent coefficient of thermal conductivity, \mathbf{x} is the position vector, and $L(\mathbf{x})$ is a function representing arbitrarily distributed heat sources (or sinks) per unit volume (or per unit area in case of a two-dimensional domain Ω). This quasi-linear elliptic partial differential equation can be subject to the Dirichlet (temperature) boundary conditions on the boundary Γ_1 ,

$$T = \bar{T} \quad (2)$$

the Neumann (heat flux Q) boundary conditions on the boundary Γ_2 ,

$$\frac{\partial \bar{T}}{\partial n} = \bar{Q} \quad (3)$$

and, when a boundary is exposed to a moving fluid, the Robin (convective heat transfer) boundary conditions on the boundary Γ_3

2.2 Numerical Formulation of the Heat Conduction Equation

When a partial differential equation is formulated numerically, an approximate solution, which is, in general, not the exact solution, must be used. Therefore, error, often called the residual, is introduced into problem. The weighted residual statement minimizes this error by setting the weighted sum of the residuals over the entire domain and in the boundary conditions to zero. For Poisson's equation, the weighted residual statement [43, 44] appears as

$$\begin{aligned} \int_{\Omega} (\nabla^2 \Theta(y) + f(y)) w(x, y) d\Omega(y) + \int_{\Gamma_1} (\Theta(y) - \bar{\Theta}(y)) \frac{\partial w(x, y)}{\partial n} d\Gamma(y) \\ - \int_{\Gamma_2} (q(y) - \bar{q}(y)) w(x, y) d\Gamma(y) = 0 \end{aligned} \quad (10)$$

where $w(x, y)$ is the weighting function, x is the real space coordinate and y is the coordinate of integration. This statement is the starting point of most numerical formulations. The difference between them lies in how the weighting function is formulated and what approximating function is used locally.

2.3 The Boundary Element Method

The Boundary Element Method (BEM) is based upon the Green's function solution procedure. It is a very efficient numerical technique [43, 44] for solving linear boundary value problems such as those governing heat conduction, elasticity, wave propagation and electromagnetic fields. We have chosen the BEM to solve most of our inverse heat conduction problems, because it has certain distinct advantages over the more common FDM, FVM and FEM. The BEM is a non-iterative and direct solution procedure which, when used for linear boundary value problems with a small number of subdomains, is significantly faster and more robust than the other numerical solution techniques. In addition, the analytic solution to the partial differential equation, in the form of the Green's function, is part of the BEM solution. Therefore, high accuracy is expected with the BEM because introducing the Green's functions does not introduce any error into the solution.

With the BEM, the dimensionality of the problem is reduced by one order such that the unknowns are strictly confined to the boundaries, Γ , of the domain, Ω . This characteristic eliminates the need for the often difficult and time-consuming task of generating an internal boundary-conforming computational grid. In the case of inverse shape design problems where the geometry changes iteratively many times during the solution process, this benefit is invaluable. And finally, the non-iterative nature of the BEM eliminates stability, reliability and convergence problems inherent to all iterative numerical methods.

2.3.1 The boundary integral equation. The BEM begins with the weighted residual statement but is used in its weak, integral formulation. Beginning with Green's second identity procedure, we integrate the first integral in the weighted residual statement (Eq. (10)) by parts twice.

$$\int_{\Omega} (\nabla^2 \Theta) w d\Omega = \int_{\Omega} (\nabla^2 w) \Theta d\Omega + \int_{\Gamma} \frac{\partial \Theta}{\partial n} w d\Gamma - \int_{\Gamma} \frac{\partial w}{\partial n} \Theta d\Gamma \quad (11)$$

We are now interested in the possibility of developing a more general method. The solution corresponding to an applied potential concentrated at a point is frequently used in boundary value problems. In the BEM, the fundamental solution, which will be represented by Θ^* , replaces the weighting function, w . The fundamental solution is a function of only the distance between the source point, y , and the observation point, x . For the two-dimensional Laplace's equation with a unit source applied at the coordinate y , the auxiliary Green's function solution equation is

$$\nabla^2 w + \delta(\mathbf{x} - \mathbf{y}) = \frac{d^2 \Theta^*}{dr^2} + \frac{1}{r} \frac{d\Theta^*}{dr} + \delta(r) = 0 \quad (12)$$

where the non-dimensional radial coordinate, r , is the distance from the source point to the observation node, $r = |\mathbf{x} - \mathbf{y}| / \ell$. Taking into consideration that, at the observation node, the governing equation for Θ^* equals the Dirac delta function, $\delta(r)$, the following Boundary Integral Equation (BIE) results [43, 44]

$$c(\mathbf{x})\Theta(\mathbf{x}) + \int_{\Gamma} q^*(\mathbf{x}, \mathbf{y}) \Theta(\mathbf{y}) d\Gamma = \int_{\Gamma} \Theta^*(\mathbf{x}, \mathbf{y}) q(\mathbf{y}) d\Gamma + \int_{\Omega} \Theta^*(\mathbf{x}, \mathbf{y}) f(\mathbf{y}) d\Omega \quad (13)$$

where

$$q^* = \frac{\partial \Theta^*}{\partial n} \quad (14)$$

The fundamental solution for the two-dimensional Laplace's equation is $\Theta^* = \ln(1/r) / 2\pi$. When the observation node \mathbf{x} is located on the boundary, Γ , the boundary integral containing the singularity must be integrated in the sense of the Cauchy principal value. Consequently, $c(\mathbf{x}) = 0$ when \mathbf{x} is outside the domain, $c(\mathbf{x}) = 1.0$ when \mathbf{x} is inside the domain, $c(\mathbf{x}) = \theta/2\pi$ when \mathbf{x} is on the boundary, where θ is the internal angle at a corner between two neighboring boundary elements so that $c(\mathbf{x}) = 0.5$ on a smooth boundary.

2.3.2 Discretization of the BIE. The boundary, Γ , of an arbitrary multiply-connected domain, Ω , can be discretized into N_{SP} boundary elements connected between N boundary nodes. One BIE can be constructed for every boundary node under consideration. The BEM solution set can then be constructed by integrating one BIE per boundary node. In addition, the domain Ω can be discretized into N_{VC} volume cells (or area cells if the domain Ω is two-dimensional) connected between N_{TOT} nodes which include the N boundary nodes and N_{VC} volume (or area) nodes. The resulting BEM solution set contains N equations with non-dimensional temperatures, Θ , and fluxes, q , unknown on the boundary only.

$$c_i \Theta_i + \sum_{k=1}^{N_{SP}} \int_{\Gamma_k} q^* \Theta d\Gamma = \sum_{k=1}^{N_{SP}} \int_{\Gamma_k} \Theta^* q d\Gamma + \sum_{k=1}^{N_{VC}} \int_{\Omega_k} \Theta^* f d\Omega \quad (15)$$

The variation of Θ and q can be assumed to be constant, linear, quadratic, etc. on each boundary element. The points where the values of non-dimensional temperature and flux are $\Theta_{k,j}$ and $q_{k,j}$, are called nodes. Since the nodes must also define the boundary discretization, the subscript k refers to the boundary element and the j index indicates the boundary element vertices (or boundary element endpoints).

First, we will elaborate on the discretization of two-dimensional domains, Ω , bounded by boundaries (contours), Γ . We have chosen to use a linear isoparametric representation for the boundary elements discretizing the one-dimensional boundaries (contour lines) Γ of the two-dimensional domains, Ω . The nodes on such boundary elements (contour elements) are numbered 1 and 2 and they are at the endpoints of each boundary element, respectively. The linear variation of the non-dimensional temperature along such a boundary element is then

$$\Theta(\xi) = \frac{1}{2}(1-\xi)\Theta_1 + \frac{1}{2}(1+\xi)\Theta_2 \quad (16)$$

with similar statements appearing for the flux, q , and the boundary coordinates x and y on the boundary Γ . The local dimensionless coordinate, ξ , follows the k th boundary element from $\xi = -1$ at endpoint 1 to $\xi = 1$ at endpoint 2. Then

$$d\Gamma = |\tilde{\mathbf{G}}| d\xi = \sqrt{\left(\frac{dx}{d\xi}\right)^2 + \left(\frac{dy}{d\xi}\right)^2} d\xi = \frac{1}{2}\sqrt{(x_2 - x_1)^2 + (y_2 - y_1)^2} d\xi \quad (17)$$

where $|\tilde{\mathbf{G}}|$ is the magnitude of the vector locally normal to the boundary, Γ .

In a similar fashion, the domain (area) cells for two-dimensional domains will be treated as isoparametric quadrilaterals where $\Theta_1, \Theta_2, \Theta_3, \Theta_4$ are values of the non-dimensional temperature at the four corners of a cell.

$$\begin{aligned} \Theta(\xi_1, \xi_2) = & \frac{1}{4}[(1-\xi_1)(1-\xi_2)\Theta_1 + (1+\xi_1)(1-\xi_2)\Theta_2 \\ & + (1+\xi_1)(1+\xi_2)\Theta_3 + (1-\xi_1)(1+\xi_2)\Theta_4] \end{aligned} \quad (18)$$

The origin of the ξ_1, ξ_2 local non-orthogonal coordinate system is located at the center of each two-dimensional quadrilateral cell so that the values of ξ_1 and ξ_2 are either +1 or -1 at the four corners of the quadrilateral cell. The domain integral must also be transformed using

$$d\Omega = |J| d\xi_1 d\xi_2 = \det \begin{bmatrix} \frac{\partial x}{\partial \xi_1} & \frac{\partial y}{\partial \xi_1} & 0 \\ \frac{\partial x}{\partial \xi_2} & \frac{\partial y}{\partial \xi_2} & 0 \\ 0 & 0 & 1 \end{bmatrix} d\xi_1 d\xi_2 \quad (19)$$

where $|J|$ is the Jacobian of the geometric transformation. After substitution, the BEM solution set (Eq. (15)) can be represented in the condensed matrix form as

$$[\text{diag}(\mathbf{c})] \{\Theta\} + [\mathbf{h}] \{\Theta\} = [\mathbf{g}] \{\mathbf{q}\} + [\mathbf{e}] \{\mathbf{f}\} \quad (20)$$

or in more detail as

$$\begin{aligned} \begin{bmatrix} c_1 & 0 & 0 \\ 0 & \ddots & 0 \\ 0 & 0 & c_N \end{bmatrix} \begin{Bmatrix} \Theta_1 \\ \vdots \\ \Theta_N \end{Bmatrix} + \begin{bmatrix} h_{1,1} & \cdots & h_{1,N} \\ \vdots & \ddots & \vdots \\ h_{N,1} & \cdots & h_{N,N} \end{bmatrix} \begin{Bmatrix} \Theta_1 \\ \vdots \\ \Theta_N \end{Bmatrix} = \begin{bmatrix} g_{1,1} & \cdots & g_{1,2N} \\ \vdots & \ddots & \vdots \\ g_{N,1} & \cdots & g_{N,2N} \end{bmatrix} \begin{Bmatrix} q_1 \\ \vdots \\ q_{2N} \end{Bmatrix} \\ + \begin{bmatrix} e_{1,1} & \cdots & e_{1,\text{NTOT}} \\ \vdots & \ddots & \vdots \\ e_{N,1} & \cdots & e_{N,\text{NTOT}} \end{bmatrix} \begin{Bmatrix} f_1 \\ \vdots \\ f_{\text{NTOT}} \end{Bmatrix} \quad (21) \end{aligned}$$

Since the non-dimensional temperature, Θ , is single-valued, the appropriate nodal values can be assembled together. In the case of a two-dimensional domain, Ω , each entry in the $[\mathbf{h}]$ matrix (Eq. (21)) has the following form

$$\begin{aligned} h_{i,j} = & \int_{-1}^1 \frac{1}{2} (1-\xi) \frac{-1}{2\pi |\mathbf{x}_i - \mathbf{y}_j(\xi)|} \hat{\mathbf{n}} \cdot \nabla |\mathbf{x}_i - \mathbf{y}_j(\xi)| |\bar{\mathbf{G}}| d\xi \\ & + \int_{-1}^1 \frac{1}{2} (1+\xi) \frac{-1}{2\pi |\mathbf{x}_i - \mathbf{y}_{j+1}(\xi)|} \hat{\mathbf{n}} \cdot \nabla |\mathbf{x}_i - \mathbf{y}_{j+1}(\xi)| |\bar{\mathbf{G}}| d\xi \quad (22) \end{aligned}$$

The unit vector, $\hat{\mathbf{n}} = \bar{\mathbf{G}}/|\bar{\mathbf{G}}|$, normal to the boundary Γ , arises from the chain rule

$$\frac{\partial \Theta^*}{\partial \mathbf{n}} = \frac{\partial \Theta^*}{\partial r} \frac{\partial r}{\partial \mathbf{n}} = \frac{\partial \Theta^*}{\partial r} \hat{\mathbf{n}} \cdot \nabla \mathbf{r} \quad (23)$$

It should be pointed out that each entry in the $[\mathbf{g}]$ matrix is kept separate because, at a corner point on the boundary, Γ , two distinct magnitudes of flux appear at the node since $\hat{\mathbf{n}}$ is discontinuous there. In other words, at a corner, the flux on one boundary element is different from the flux on the neighboring boundary element, although they possess the same corner coordinates. Thus, a total of $2N$ fluxes appear in the discretized form of the BIE because for two-dimensional domains, Ω , there are the same number of boundary elements as there are boundary nodes.

The development of the BIE for three-dimensional problems is identical to the two-dimensional case except the fundamental solution is $\Theta^* = 1/4\pi r$. The boundary (surface), Γ , of the three-dimensional domain (volume), Ω , can be discretized into either triangular or quadrilateral boundary elements (surface panels). The domain (volume) can be discretized into tetrahedral or hexahedral cells. In three-dimensional problems, we have chosen to use isoparametric quadrilateral surface panels and hexahedral volume cells because of their structured nature.

2.3.3 Singular integrals. The integrals $h_{i,j}$ and $g_{i,k}$ can be calculated using the simple Gauss quadrature rule for all boundary elements except the two integrals where the observation node is at one of the vertices of the boundary element being integrated (a singularity). For two-dimensional problems with linear isoparametric elements, these integrals can be easily computed analytically. The $h_{i,i}$ term is identically zero because the vectors \hat{n} and \hat{r} are orthogonal over the boundary element when the observation node is on the boundary element. The $[g]$ integrals (Eq. (21)) can be calculated analytically when the observation node is at vertex 1 or at vertex 2 as follows

$$g_{1,k,1} = \frac{s}{2} \left(\frac{3}{2} - \ln(s) \right) \quad \text{and} \quad g_{1,k,2} = \frac{s}{2} \left(\frac{1}{2} - \ln(s) \right) \quad (24)$$

where the length of the boundary element is $s = \sqrt{(x_2 - x_1)^2 + (y_2 - y_1)^2}$.

A similar situation arises in three-dimensional problems when the volume cell contains a singularity at one of its vertices. Since this integral cannot be computed analytically, an integral transformation rule is recommended [45]. A cubic variable transformation is valid for any location of the singular point. Each variable of integration, ξ_ℓ , is thus represented in terms of a new variable, γ , as

$$\xi_\ell = a\gamma^3 + b\gamma^2 + c\gamma + d \quad (25)$$

subject to the following requirements

$$\left. \frac{d^2 \xi_\ell}{d\gamma^2} \right|_{\bar{\xi}} = 0 \quad \left. \frac{d \xi_\ell}{d\gamma} \right|_{\bar{\xi}} = 0 \quad \xi_\ell(1) = 1 \quad \xi_\ell(-1) = -1 \quad (26)$$

Here, the subscript ℓ assumes different values as follows: $\ell = 1$ for contour integration; $\ell = 1$ and 2 for area (surface) integration; $\ell = 1, 2$ or 3 for volume integration. Also, $\bar{\xi}$ is the location of the singular point in the local coordinate system. A solution to this problem is given by

$$a = \frac{1}{1 + 3\bar{\gamma}^2} \quad b = \frac{-3\bar{\gamma}}{1 + 3\bar{\gamma}^2} \quad c = \frac{3\bar{\gamma}^2}{1 + 3\bar{\gamma}^2} \quad d = -b \quad (27)$$

where $\bar{\gamma}$ is the value of γ which satisfies $\xi_\ell(\bar{\gamma}) = \bar{\xi}$, calculated by

$$\bar{\gamma} = \sqrt[3]{\bar{\xi}(\bar{\xi}^2 - 1) + |\bar{\xi}^2 - 1|} + \sqrt[3]{\bar{\xi}(\bar{\xi}^2 - 1) - |\bar{\xi}^2 - 1|} + \bar{\xi} \quad (28)$$

2.3.4 Application of boundary conditions. For a well-posed boundary value problem, every point on the boundary is given either one Dirichlet, one Neumann, or one Robin-type boundary condition. At the same time, the interior heat source function must be known. The known heat source function, $\{f\}$, can be multiplied by its coefficient matrix, $[e]$, to form the known vector $\{p\}$. The term

$[\text{diag } \mathbf{c}]$ can be absorbed into the diagonal of the matrix $[\mathbf{h}]$ to form matrix $[\tilde{\mathbf{h}}]$. Equation (20) then results in the following matrix form

$$[\tilde{\mathbf{h}}] \{\Theta\} = [\mathbf{g}] \{\mathbf{q}\} + \{\mathbf{p}\} \quad (29)$$

The computation of the free term $[\text{diag } \mathbf{c}]$ can be simplified. Rather than computing the geometric internal angle at the i th boundary node, the diagonal of the $[\tilde{\mathbf{h}}]$ matrix can be computed implicitly by considering what would happen if the temperature was constant everywhere and no heat sources were present. In this instance, fluxes would be identically zero. The diagonal, being the only unknown term in this case, can be computed by summing the remaining terms in the BIE so that

$$\tilde{h}_{ii} = - \sum_{j=1}^N \tilde{h}_{ij} \quad (30)$$

In the well-posed steady state problems the boundary conditions may be multiplied out and carried to the right-hand-side and added to $\{\mathbf{p}\}$ to form a vector of knowns, $\{\mathbf{F}\}$, while the left-hand side remains in the standard form $[\mathbf{A}]\{\mathbf{X}\}$. Thus, the entire BIE method reduces to a linear algebraic system of the standard form

$$[\mathbf{A}]\{\mathbf{X}\} = \{\mathbf{F}\} \quad (31)$$

The equation set that will result has N unknowns and N equations. It is a well-posed system of linear algebraic equations that can be solved for the unknown vector $\{\mathbf{X}\}$ by any appropriate matrix solver.

3 STEADY INVERSE HEAT CONDUCTION PROBLEMS

3.1 Determination of Steady Thermal Boundary Conditions

Inverse determination of unknown steady thermal boundary conditions when temperature and heat flux data are not available on certain boundaries is an ill-posed problem [2–6]. In this case, additional overspecified measurement data involving both temperature and heat flux are required on some other, more accessible boundaries or at a finite number of points within the domain. For example, if at all four vertices of a quadrilateral cell the heat sources are known, at two vertices both $\Theta = \bar{\Theta}$ and $q = \bar{q}$ are known, while at the remaining two vertices neither Θ or q is known, the BIE (Eq. (29)) begins as

$$\begin{bmatrix} \tilde{h}_{11} & \tilde{h}_{12} & \tilde{h}_{13} & \tilde{h}_{14} \\ \tilde{h}_{21} & \tilde{h}_{22} & \tilde{h}_{23} & \tilde{h}_{24} \\ \tilde{h}_{31} & \tilde{h}_{32} & \tilde{h}_{33} & \tilde{h}_{34} \\ \tilde{h}_{41} & \tilde{h}_{42} & \tilde{h}_{43} & \tilde{h}_{44} \end{bmatrix} \begin{bmatrix} \bar{\Theta}_1 \\ \bar{\Theta}_2 \\ \bar{\Theta}_3 \\ \bar{\Theta}_4 \end{bmatrix} = \begin{bmatrix} g_{11} & g_{12} & g_{13} & g_{14} \\ g_{21} & g_{22} & g_{23} & g_{24} \\ g_{31} & g_{32} & g_{33} & g_{34} \\ g_{41} & g_{42} & g_{43} & g_{44} \end{bmatrix} \begin{bmatrix} \bar{q}_1 \\ q_2 \\ \bar{q}_3 \\ q_4 \end{bmatrix} + \begin{bmatrix} p_1 \\ p_2 \\ p_3 \\ p_4 \end{bmatrix} \quad (32)$$

In order to solve this set, all of the unknowns will be collected on the right-hand side, while all of the knowns are assembled on the left. A simple algebraic manipulation yields the following set:

$$\begin{bmatrix} \tilde{h}_{12} & -g_{12} & \tilde{h}_{14} & -g_{14} \\ \tilde{h}_{22} & -g_{22} & \tilde{h}_{24} & -g_{24} \\ \tilde{h}_{32} & -g_{32} & \tilde{h}_{34} & -g_{34} \\ \tilde{h}_{42} & -g_{42} & \tilde{h}_{44} & -g_{44} \end{bmatrix} \begin{Bmatrix} \Theta_2 \\ q_2 \\ \Theta_4 \\ q_4 \end{Bmatrix} = \begin{bmatrix} -\tilde{h}_{11} & g_{11} & -\tilde{h}_{13} & g_{13} \\ -\tilde{h}_{21} & g_{21} & -\tilde{h}_{23} & g_{23} \\ -\tilde{h}_{31} & g_{31} & -\tilde{h}_{33} & g_{33} \\ -\tilde{h}_{41} & g_{41} & -\tilde{h}_{43} & g_{43} \end{bmatrix} \begin{Bmatrix} \bar{\Theta}_1 \\ \bar{q}_1 \\ \bar{\Theta}_3 \\ \bar{q}_3 \end{Bmatrix} + \begin{Bmatrix} p_1 \\ p_2 \\ p_3 \\ p_4 \end{Bmatrix} \quad (33)$$

Since the entire right-hand side is known, it may be reformulated as a vector of knowns, $\{F\}$. The left-hand side remains in the form $[A]\{X\}$. Also, additional equations may be added to the equation set if, for example, temperature or heat flux measurements are known at certain locations within the domain. In general, the geometric coefficient matrix $[A]$ will be non-square and highly ill-conditioned. Most matrix solvers will not work well enough to produce a correct solution.

3.2 Truncated Singular Value Decomposition

There exists a very powerful technique for dealing with sets of equations that are either singular or very close to singular. These techniques, known as Singular Value Decomposition (SVD) methods [39, 29, 46–50], are widely used in solving most linear least squares problems. The goal of the SVD is to choose a solution vector $\{X\}$ so as to minimize the error

$$E = \|\{F\} - [A]\{X\}\| \quad (34)$$

which is the distance from the point $\{F\}$ to the point $[A]\{X\}$ in the column space. Thus, the solution vector $\{X\}$ is the projection of $\{F\}$ onto the subspace which the column vectors of $[A]$ define. Any $M \times N$ matrix $[A]$ can be written as the product of an $M \times N$ column-orthogonal matrix, $[U]$, an $N \times N$ diagonal matrix $[W]$ with positive singular values, and the transpose of an $N \times N$ orthogonal matrix $[V]$.

$$[A] = [U] \begin{bmatrix} w_1 & 0 & 0 \\ 0 & \ddots & 0 \\ 0 & 0 & w_N \end{bmatrix} [V] \quad (35)$$

The singular values, w_1, \dots, w_N , are the eigenvalues of a matrix $[A]^T[A]$. The columns of $[U]$ corresponding to the nonzero singular values, w_j , make the orthonormal set of basis vectors that span the range of $[A]$. The columns of $[V]$ corresponding to the zero singular values, w_j , are an orthonormal basis for the nullspace. If the matrix $[A]$ is singular, then there is some subspace of $\{X\}$, called the nullspace, that is mapped to zero, that is, $[A]\{X\} = \{0\}$. Since $[U]$ and $[V]$ are each orthogonal in the sense that their columns are orthonormal, the solution vector can be easily found as

$$\{X\} = [V][\text{diag}(1/w_j)]([U]^T\{F\}) \quad (36)$$

For a well-conditioned matrix, the singular values w_j will be roughly of the same order of magnitude. The condition number of a matrix is defined as w_{\max}/w_{\min} . As the condition number increases, the matrix becomes more ill-conditioned. The LU factorization and Gaussian elimination may give a formal solution to an ill-conditioned set of equations, but the solution vector will have highly oscillating components whose algebraic cancellation, when multiplied by the matrix $[A]$, gives a very poor approximation to the vector $\{F\}$. Eliminating very

small singular values has the effect of removing those algebraic terms that, because they are dominated by noise and round-off error, produce the oscillating solution vector. In order to determine which singular values are to be eliminated, we must choose a parameter, τ , as a singularity magnitude threshold. Any singular value that satisfies $w_j/w_{\max} < \tau$ is zeroed out. In order to zero-out a singular value, one should simply replace the $1/w_j$ by zero. The zeroing of a small singular value corresponds to throwing away one linear combination from the set of equations that is so corrupted by round-off error as to be at best useless. For each particular problem, there is a range of threshold values where the algorithm will produce a correct solution. A choice of the threshold outside of this range will yield another solution vector whose direction is very nearly the nullspace vector. Since the SVD algorithm is capable of solving non-square matrices, the number of unknowns in the equation set need not be the same as the number of equations. Thus, virtually any combination of boundary conditions and internal temperature measurements will yield at least some solution.

3.3 Tikhonov's Regularization

Tikhonov regularization [37, 29] is another type of single-parameter minimization where the solution vector $\{X\}$ minimizes the weighted sum of the norm of the error vector defined by Tikhonov as

$$E = \| \{F\} - [A]\{X\} \| + \lambda \| \{X\} \| \quad (37)$$

where λ is the Tikhonov's regularization parameter. We find a minimum error norm by differentiating this equation with respect to each component of the unknown vector, $\{X\}$, and setting the result equal to zero. After substituting the singular value decomposition and solving for the unknown vector $\{X\}$, the resulting formulation is as follows

$$\{X\} = [V]([W]^T[W] + \lambda[I])^{-1}[W]^T[U]\{F\} \quad (38)$$

where $[I]$ is the identity matrix. Tikhonov regularization is a generalization of least-squares truncation, but instead of simply eliminating terms associated with small singular values, they are weighted by a factor $(1 + \lambda/w^2)$. A low value of λ makes the residual term $[A]\{X\} - \{F\}$ smaller, approaching the least squares solution. Because of the destabilizing effect of the small singular values, the solution for an ill-conditioned matrix oscillates erratically. Larger Tikhonov regularization parameters act as a filter to gradually reduce the effect of the singular values because w_j/w_{\max} are less than λ . Thus, the optimal choice of λ provides a balance between the accuracy and the smoothness of the solution. Tikhonov suggested that λ can be found based upon knowledge of the measurement errors [29], that is, λ should be chosen when the least sum of squares lies between

$$[N_T - \sqrt{2N_T}] \sigma^2 \quad \text{and} \quad [N_T + \sqrt{2N_T}] \sigma^2 \quad (39)$$

where N_T is the number of temperature measurements and σ^2 is the variance of those measurements.

The level of discretization was found to have no effect on the optimum SVD threshold value, τ_{opt} [9]. The effective range of τ that produced the minimum variance and bias for all levels of discretization was $0.004 \leq \tau \leq 0.08$.

On the other hand, the level of discretization had some influence on Tikhonov's regularization scheme. After the BEM matrices are integrated and the singular value decomposition computed, an iterative quadratic optimization algorithm can be employed [9] in order to determine λ_{opt} . The value of λ can be allowed to vary while the cost function

$$F(\lambda) = w_{\text{var}} \sigma_{\Theta}^2 + w_{\text{bias}} \left(\Theta_{\text{mean}} - \Theta_{\text{analytic}} \right)^2 \quad (40)$$

is minimized. Here, w_{var} and w_{bias} are user-specified weighting coefficients for the variance, σ_{Θ}^2 , and the bias in the non-dimensional temperature. With $w_{\text{var}} = w_{\text{bias}} = 1$, the optimum Tikhonov's regularization parameter, λ_{opt} , is usually found in 5 to 10 computationally inexpensive iterations [9].

3.4 Results of BEM for Unknown Thermal Boundary Conditions

The accuracy and versatility of the BEM in determining the unknown steady state temperatures and heat fluxes on the boundaries of two- and three-dimensional multiply-connected domains is demonstrated in the following examples. Notice that evaluation of the unknown local values of heat convection coefficient (Eq. (4)) is trivial once the local surface temperature and normal temperature derivative are predicted.

3.4.1 Rectangular plate and finite rod. The accuracy of the BEM as a solution to the two- and three-dimensional steady state ill-posed problem was verified for a rectangular flat plate and a rod having square cross section. The rectangular plate was 6.0 m long by 1.0 m wide. The rod was 6.0 m long by 1.0 m by 1.0 m thick. Thermal conductivity was chosen as $k = 1.0 \text{ W m}^{-1} \text{ K}^{-1}$ and there were no heat sources, that is, $L = 0$. The long sides of the plate and rod were specified to be adiabatic ($-k\bar{Q} = 0 \text{ W m}^{-2}$) while at one end, the boundary conditions were overspecified with a temperature of $\bar{T} = 300.0 \text{ K}$ and a heat flux of $-k\bar{Q} = -50.0 \text{ W m}^{-2}$. The boundary at the opposite end was considered to be inaccessible and, as such, both temperature and heat flux were unknown there. The rectangular plate was discretized with 14 linear elements (6 per each of the two sides and 1 on each end). The rod surface was discretized with 26 square flat panels (6 per each of the four sides and 1 on each end). Both two- and three-dimensional BEM numerical formulations of the UIHCP were highly successful in computing a linear temperature field within the rod that was accurate to almost the floating point precision of the computer. The predicted temperatures and heat fluxes at the end of the plate and the rod (where no boundary conditions were given) were $\bar{T} = 0.00001 \text{ K}$ and $-k\bar{Q} = -49.99997 \text{ W m}^{-2}$, respectively, compared to the analytic solutions of $\bar{T} = 0 \text{ K}$ and $-k\bar{Q} = -50.0 \text{ W m}^{-2}$.

3.4.2 Annular disk. The behavior of the BEM algorithm for various combinations of boundary conditions can be demonstrated for steady-state heat conduction in a two-dimensional, annular, concentric circular disk with no heat

sources [2, 3]. In the well-posed (analysis or direct or forward) case of no heat sources and constant temperatures imposed on the entire outer and inner circular boundaries, the analytic solution for the resulting Laplace's equation for the Kirchhoff's non-dimensional temperature is easily found as

$$\Theta(\rho) = c_1 + c_2 \ln \rho \quad (41)$$

where $\rho = r/\ell$. In our test case, the non-dimensionalized outer radius of the annular disk was $\rho_{\text{outer}} = 1.2$ and the centrally located circular hole had a non-dimensional radius of $\rho_{\text{inner}} = 0.5$. The analytic solution for a well-posed Dirichlet analysis problem was obtained by applying $\bar{\Theta}_{\text{outer}} = 1.0$ on the outer circular boundary and $\bar{\Theta}_{\text{inner}} = 0.5$ on the inner circular boundary of the annular domain. For these parameters the analytic values of the integration constants were $c_1 = 0.8959$ and $c_2 = 0.5712$. The corresponding analytic values of the radial non-dimensional heat fluxes are $\bar{q}_{\text{outer}} = 0.4759$ and $\bar{q}_{\text{inner}} = 1.1422$. The accuracy of our BEM algorithm in its analysis mode was verified on the same test case. The geometry was discretized with 36 equal-length linear isoparametric boundary elements on each outer and inner circular boundary. The BEM program predicted the non-dimensional temperature in the entire annular domain which averaged only a 0.1% negative bias error and 0.0001 standard deviation versus the analytic solution.

In order to study the feasibility and accuracy of the BEM solution to the steady inverse heat conduction problem (SIHCP), four variations of the given problem were performed and the results obtained were compared to the analytic solution. In all the test cases, a constant temperature was specified on the entire outer circular boundary. At the same time, both temperature and the heat flux were treated as unknown on the entire inner circular boundary. The test cases are summarized in Table 1.

Test 1. The entire outer boundary was overspecified with constant flux boundary conditions. The BEM computed the non-dimensional temperature field within the annular domain in addition to the unknown non-dimensional temperatures and heat fluxes on the inner boundary. The computed isotherms (Fig. 1a) for the annular solid disk demonstrate an almost perfectly symmetric result with an average error of 0.5% in non-dimensional temperature and a somewhat oscillating error in heat flux averaging about -1.5%.

Test 2. The heat flux boundary conditions were overspecified on the outer circular boundaries of the first and third quadrants only. The computed non-dimensional temperature distribution on the inner boundary was somewhat oscillatory (Fig. 1b), but averaged only a 0.75% error. The predicted heat flux on the inner boundary averaged an error of about -2.0%.

Test 3. The heat flux boundary conditions were overspecified only on the upper half of the outer circular boundary. The computed non-dimensional temperature field is asymmetric about the horizontal centerline (Fig. 1c), but shows a nearly perfect symmetry about the vertical centerline. The error of the predicted non-dimensional temperature on the inner boundary peaks to 24%. The errors in computed fluxes peak to about 40% at the point farthest from the overspecified data.

Test 4. The heat flux boundary conditions were overspecified on the outer boundary of the first quadrant only. The error in the predicted non-dimensional temperature field worsens as the distance from the overspecified data increases (Fig. 1d) and peaks to 60% at the point farthest from the overspecified data. Notice

also that the predicted non-dimensional temperature field is symmetric about the line inclined 45 degrees and passing through the center of the circle.

Table 1 Important parameters for the annular disk SIHCP cases

Test case	Number of known values (Θ and q)	Number of unknown values (Θ and q)	Number of algebraic equations
1	72	72	72
2	54	90	72
3	54	90	72
4	45	99	72

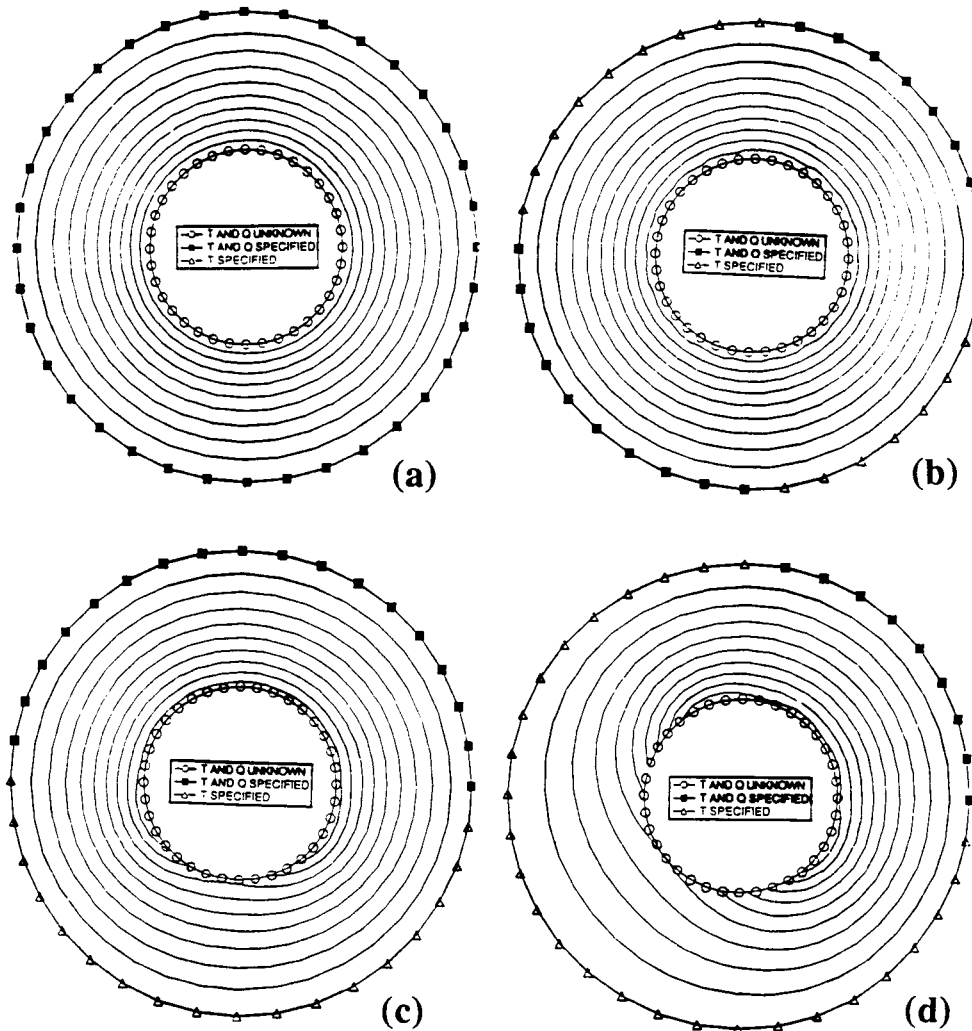
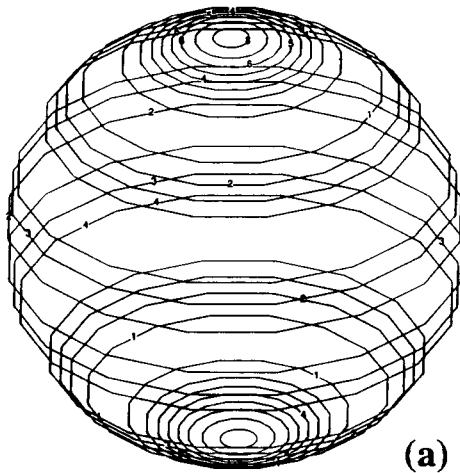


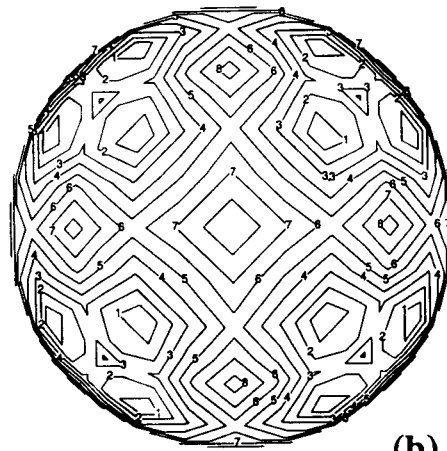
Figure 1 Isotherms predicted with the inverse BEM in an annular circular disk with specified constant temperature only (triangles) and both temperature and heat flux (full squares). Nothing was specified on the entire inner circular boundary (circles). The over-specified boundary conditions were on (a) the entire outer boundary, (b) the first and the third quadrant of the outer boundary, (c) the upper half of the outer boundary, and (d) the first quadrant of the outer boundary.



(a)

Level	T
8	58.3164
7	56.7609
6	55.2053
5	53.6498
4	52.0942
3	50.5387
2	48.9831
1	47.4276

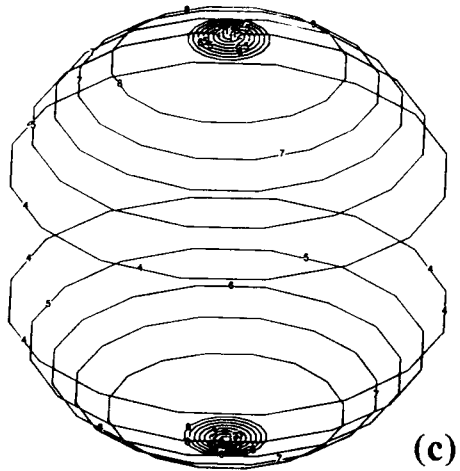
Level	Flux
8	-172.063
7	-172.626
6	-173.19
5	-173.753
4	-174.317
3	-174.88
2	-175.444
1	-176.007



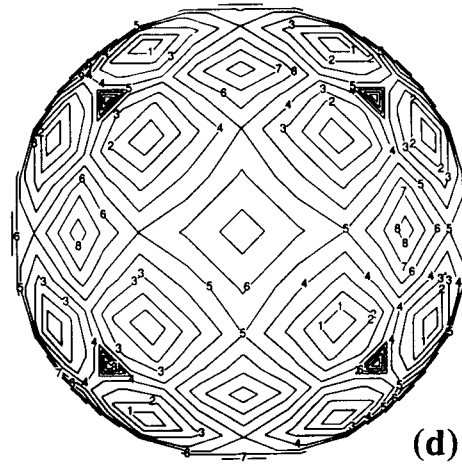
(b)

Level	T
8	52.154
7	51.607
6	51.06
5	50.513
4	49.966
3	49.419
2	48.872
1	48.325

Level	Flux
8	-128.678
7	-140.256
6	-151.833
5	-163.411
4	-174.989
3	-186.567
2	-198.144
1	-209.722



(c)



(d)

Figure 2 Thermal boundary conditions predicted on the surface of a spherical cavity when temperature and heat flux were specified on the entire outer spherical boundary and nothing was specified on the concentric spherical cavity. Isotherms predicted with a meridional surface grid (a) and a cube-to-a-sphere expanded grid (b) and fluxes predicted with a meridional surface grid (c) and a cube-to-a-sphere expanded grid (d) .

3.4.3 Sphere within a sphere. The BEM solution to the SIHCP was also exercised on a simple three-dimensional geometry consisting of a sphere of radius $r = 1.2$ m with a concentric spherical cavity of radius $r = 0.5$ m. With $k = 1.0$ W $m^{-1} K^{-1}$, $\bar{T}_{outer} = 100.0$ K, $\bar{T}_{inner} = 50.0$ K, and $L = 0$, the analytic solution is $T(r) = c_1 + c_2/r$ where $c_1 = 135.72$ K and $c_2 = -42.86$ K m. We then used isoparametric bilinear quadrilateral panels to discretize the spherical boundaries [3]. The surface grids were used at various levels of refinements, including 8, 10, 12 and 16 boundary elements (panels) both longitudinally and latitudinally on the outer and inner spherical boundary. The analysis version of the BEM solved for the fluxes, Q , on the outer and inner spherical boundaries. The numerical result contained a biased error of 2% that was concentrated at the poles for all levels of grid refinement.

The SIHCP problem was then formulated by overspecifying the outer spherical boundary (applying both temperature and flux from the analytic solution), while not providing any thermal boundary conditions on the inner (cavity) spherical boundary. The BEM-predicted temperatures (Fig. 2a) and heat fluxes (Fig. 2b) on the surface of the spherical cavity, with the discretization of 16×16 quadrilateral bilinear panels, illustrate biased errors up to 16% in temperature and 3% in heat flux

at the poles since the analytic solution is $-k\bar{Q}_{inner} = -171.44$ W m^{-2} . The error of the SIHCP was the greatest at the poles because the boundary grid of bilinear quadrilateral cells deforms to nearly triangular cell shapes adjacent to the poles. These boundary cells behave very poorly because the approximating polynomials are not well-behaved in these regions. In addition, it is difficult to carry out the integration over these polar surface integrals properly due to the nature of the singular fundamental solution. Moreover, when observation nodes are very close to the boundary element of integration, the accuracy of the numerical quadrature integration scheme deteriorates.

We then repeated the SIHCP with a different surface grid pattern. First, a cube was discretized with 16 bilinear quadrilateral boundary elements on each of its six sides. A cubical hole centered within the first cube was discretized with the same type of grid. The surface grids of both cubes were then expanded radially to a sphere-within-a-sphere configuration. The same SIHCP was then solved using our BEM algorithm with Tikhonov's regularization parameter $\lambda = 1.0 \times 10^{-12}$. This provided a slightly better result than the SVD matrix solver for the predicted temperatures on the surface of the spherical cavity. These results show a maximum unbiased error in temperature of about 4% (Fig. 2c). The errors in fluxes were quite large (Fig. 2d), maximizing to 22% at what would be the corners of the original cubical cavity. The results did not improve or worsen for other levels of discretization. During the expansion of the cube-within-a-cube grid into a sphere-within-a-sphere grid the quadrilateral cells are stretched adjacent to what used to be the corner nodes of the cubes. The BEM is sensitive to geometric distortions in isoparametric elements. The Jacobian of the nearly triangular boundary elements was found to be almost zero at the vertices of these elements. Other isoparametric boundary elements such as triangles and higher-order quadrilaterals should be attempted to remedy this problem.

3.4.4 Treatment of geometries with corners. The accuracy of the ill-posed BEM formulation was shown (Figs. 1c–1d) to deteriorate as the amount of overspecified data decreases and when the distance from the overspecified data increases. We have also noticed that the accuracy of this approach deteriorates when only Dirichlet boundary conditions are specified across a sharp corner.

In the implementation of the direct BEM for the solution of the heat conduction equation, the heat flux at a corner is double-valued due to the non-

uniqueness of the outward normal. This fact poses a numerical problem at nodes located at these corners. There are three variables at such nodes, the temperature and two normal temperature derivatives, and only one boundary integral equation is available. Dirichlet boundary conditions provide only one of the three unknowns for each corner node. When the corner node is on an inaccessible boundary, nothing is provided there. In these cases, one additional equation must be provided. This condition can be satisfied using the discontinuous element formulation [43, 44] or by developing an expression that relates the normal and tangential temperature derivatives to a unique temperature gradient [51]. Although these approaches work well in the analysis of well-posed problems, difficulties arise when the ill-posed or inverse problems are encountered. So far, we have found no universally adequate formulation for the accurate treatment of corners for the ill-posed problem.

As an example of the properly treated corners, a well-posed problem was constructed for the geometry of a cross-shaped hole within a square plate with $f = 0$. The outer boundary of the square plate was specified with $\bar{\Theta}_{\text{outer}} = 1.0$ and the inner, cross-shaped boundary was specified with $\bar{\Theta}_{\text{inner}} = 0$. The outer and the inner boundary were discretized with 60 linear isoparametric equal-length boundary elements, respectively. The results of the BEM analysis of this well-posed Dirichlet problem (without $f = 0$) are shown as a plot of computed isotherms (Fig. 3a).

Next, the fluxes on the outer square boundary that were computed by the analysis BEM solution were applied in addition to $\bar{\Theta}_{\text{outer}} = 1.0$ as overspecified boundary conditions. This time, nothing was specified on the boundary of the cross-shaped hole. The BEM developed a solution to this SIHCP. The predicted non-dimensional temperature field around the cross-shaped hole appear to have been predicted quite accurately (Fig. 3b).

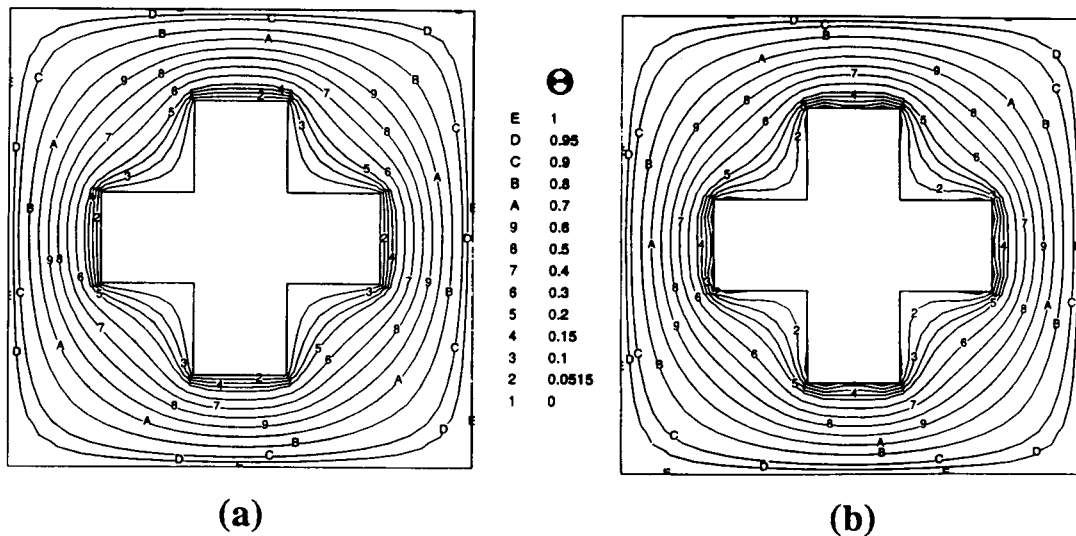


Figure 3 Isotherms predicted using BEM in a square plate with a cross-shaped central hole. Well-posed problem (temperatures given on both entire inner and outer boundaries) results (a) and inverse problem (temperatures and heat fluxes given on the outside boundary and nothing provided on the boundaries of the cross-shaped hole) results (b).

3.4.5 Two-dimensional section of a cooled rocket chamber wall. The ill-posed BEM formulation was attempted on a realistic engineering design problem with temperature-dependent material properties. High pressure, reusable rocket thrust chambers encounter progressive thinning of the coolant passage wall after repetitive engine operation [52]. This deformation is caused by high thermal plastic deformations and recrystallization that eventually cause cracks to form in the coolant passage wall. An engineer who wishes to reduce or eliminate the plastic strain by reshaping the coolant flow passage may obtain experimental data such as nozzle shroud temperatures and heat fluxes. Unfortunately, the engineer cannot obtain data within a coolant flow passage due to the extremely low temperature of the liquid hydrogen coolant and the small dimensions of the passages.

The hot gas wall (left boundary in Fig. 4a) was specified with $-k\bar{Q}_{\text{hot}} = -57.24 \times 10^6 \text{ W m}^{-2}$. The outer shroud (right boundary in Fig. 4a) heat flux was assumed to be negligible ($\bar{Q}_{\text{outer}} = 0$). The shroud was overspecified with a temperature of $\bar{T}_{\text{outer}} = 288.0 \text{ K}$ taken from experimental measurements [52] and there were no heat sources ($f = 0$). The circumferentially-periodic meridional boundaries of the nozzle wall section (top and bottom boundaries in Fig. 4a) were also specified to be adiabatic ($\partial\bar{T}/\partial\theta = 0$).

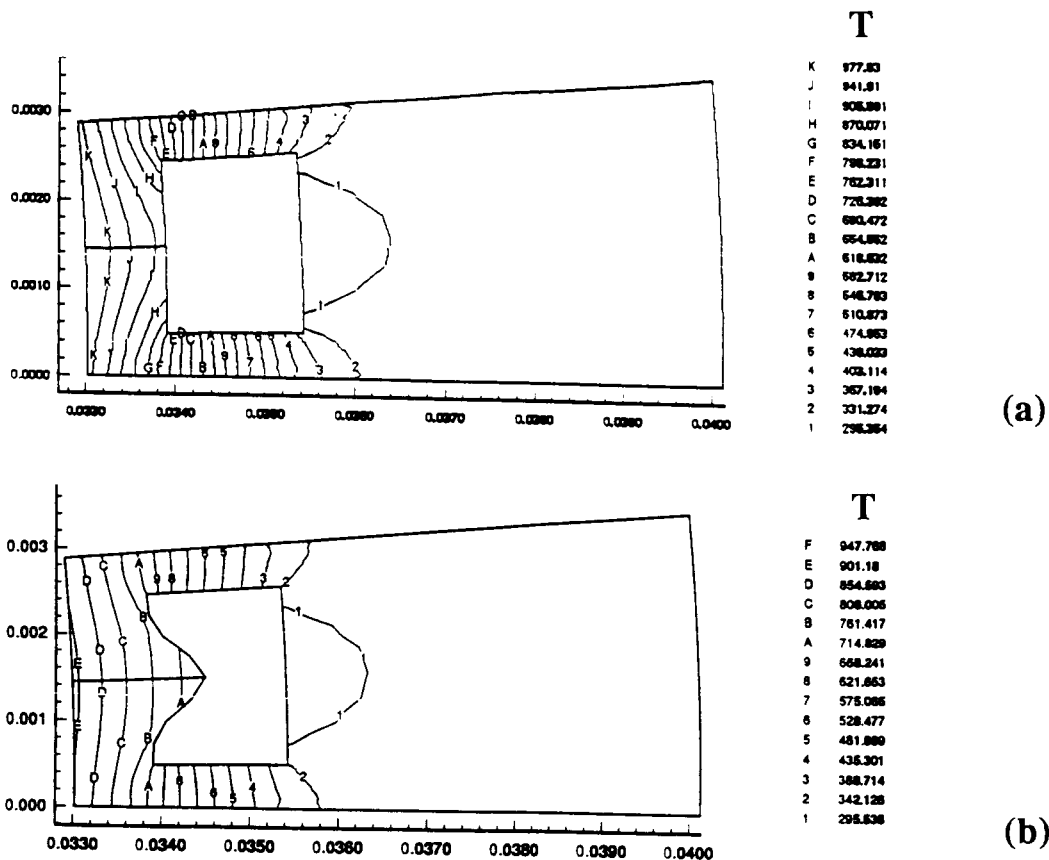


Figure 4 Isotherms predicted inside a circumferentially-periodic segment of a rocket nozzle wall with a cooling channel when nothing was known on the boundaries of the cooling channel. Results of the inverse boundary condition code for a rectangular channel (a) and for a channel with a rounded fin (b).

The coefficient of thermal conductivity of the metal was $k(T) = k_0 (a + bT)$, where $k_0 = 365.6 \text{ W m}^{-1} \text{ K}^{-1}$, $a = 1.0$ and $b = -3.059 \times 10^{-5} \text{ K}^{-1}$. The shroud was discretized with 8, the throat section with 16, and each of the meridional boundaries with 8 linear isoparametric boundary elements. The coolant flow passage (hole) perimeter was discretized with 40 linear isoparametric boundary elements. The resulting BEM formulation of the SIHCP contained 48 knowns, 112 unknowns and 80 equations. The predicted isotherms within the solid region of the nozzle wall section are illustrated in Fig. 4a. These results [5] show a symmetry about the radial line passing through the center of the coolant passage. Notice also that the predicted temperatures are very high along the left wall of the coolant passage close to the nozzle throat surface.

Next, a thick fin, shaped like a sine-wave, was added to the left wall [5] of the coolant passage. The predicted isotherms for this SIHCP (Fig. 4b) demonstrate that even a seemingly minor shape alteration can produce a significant decrease of the temperature on the hot side of the coolant passage and the nozzle throat surface. Such a simple shape alteration can also effectively spread the isotherms, thus reducing the thermal stress concentration. This calculation consumed 45 seconds on a personal computer with 100MHz clock speed (or a fraction of a second on Cray-YMP computer) although we used SVD matrix algorithm.

3.4.6 Three-dimensional cooled rocket engine chamber. Our three-dimensional BEM code was also exercised on a realistic engineering problem with multiple regions having significantly different heat conductivities [6]. A three-dimensional circumferentially-periodic segment of the already described rocket thrust chamber wall containing a coolant passage was used as a test case for our three-dimensional BEM code where temperatures and heat fluxes on the walls of the coolant passage were treated as unknown. The hot gas wall was specified with a

heat flux $-k\bar{Q}_{\text{hot}} = -100 \times 10^6 \text{ W m}^{-2}$. The outer boundary temperature of $\bar{T}_{\text{outer}} = 140 \text{ K}$ was taken from experimental measurements [56]. The circumferential periodicity of the 72 cooling passages was assumed to exist. Consequently, meridional boundaries of the chamber wall section were specified to be adiabatic. Similarly, front and end walls of the three-dimensional periodic chamber section were assumed to be adiabatic. The chamber was 0.154 m long [56]. Liquid hydrogen was assumed to have an average bulk temperature of $T_{\text{amb}} = 50 \text{ K}$ and the constant heat convection coefficient $h = 1 \times 10^5 \text{ W m}^{-2} \text{ K}^{-1}$ was specified on the coolant passage walls. The hot throat surface was coated with a thin layer of zirconium-oxide ($k = 8.0 \text{ W m}^{-1} \text{ K}^{-1}$). The next layer was made of nickel-chromium ($k = 23.0 \text{ W m}^{-1} \text{ K}^{-1}$), while the bulk of the combustion chamber was made of copper ($k = 378.0 \text{ W m}^{-1} \text{ K}^{-1}$). The outer coating layer was made of a copper closeout ($k = 385.0 \text{ W m}^{-1} \text{ K}^{-1}$).

The well-posed (direct or analysis) problem was formulated first, where the constant heat convection coefficient, h_{hole} , was specified on the coolant flow passage walls, \bar{Q}_{hot} was specified on the hot gas wall, \bar{T}_{outer} was specified on the outer surface of the chamber, and $(\partial T / \partial \theta) = 0$ on the meridional periodic surfaces. The computed surface isotherms are depicted in Figure 5a. Then, an ill-posed (inverse) problem was created by pretending that nothing is known on the walls of the cooling passage, while enforcing on the hot gas surface both the already known \bar{Q}_{hot} and the \bar{T}_{hot} that was obtained from the analysis solution.

Similarly, overspecified data was provided at the outer surface of the chamber by enforcing an already known \bar{T}_{outer} and the \bar{Q}_{outer} that was obtained from the analysis solution. The comparison of the computed surface isotherms from the direct (Fig. 5a) and inverse (Fig. 5b) BEM shows a reasonably good agreement despite the coarse grid used in this test case and the widely disparate thermal conductivities.

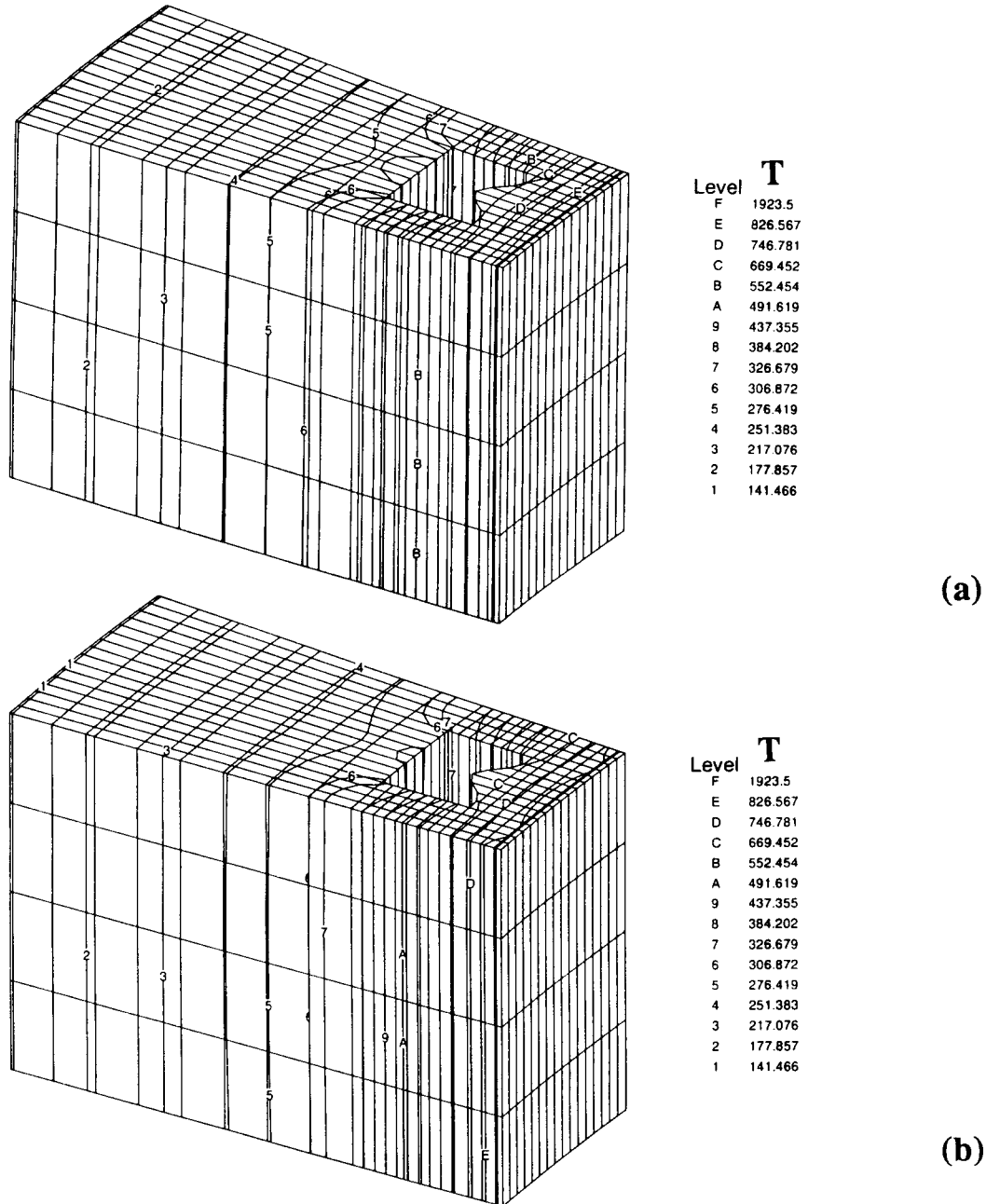


Figure 5 Surface isotherms predicted on a circumferentially-periodic three-dimensional segment of a rocket chamber wall with a cooling channel made of four different materials: a) direct problem, b) inverse boundary condition problem

3.4.7 Annular disk with known internal heat generation. In order to verify the accuracy of our BEM code when solving the Poisson's equation, we first chose to solve a well-posed steady axisymmetric heat conduction problem in an annular circular disk with radially varying heat source function [8]. Since the non-dimensional boundary conditions and the heat generation are axisymmetric, the analytic solution of Eq. (6) is simple to obtain as

$$\Theta(\rho) = - \int_0^{\rho} \left[\frac{1}{\rho} \int_0^{\rho} f(\rho) \rho d\rho \right] d\rho + c_1 \ln \rho + c_2 \quad (42)$$

With $f = \text{constant}$, the analytic solution is $\Theta(\rho) = -f\rho^2/4 + c_1 \ln \rho + c_2$. We decided to use $\bar{\Theta}_{\text{outer}} = 0$, $\bar{\Theta}_{\text{inner}} = 0$, and $f = 1.0$ which results in $c_1 = 0.3398$ and $c_2 = 0.298$. The numerical BEM solution was then compared to this analytic solution with the same circular disk geometry and well-posed boundary conditions. Both inner and outer circular boundaries were discretized with 36 equal-length, linear, isoparametric boundary elements and the annular domain was discretized with 36×10 quadrilateral bilinear isoparametric cells. The relative errors for the non-dimensional temperature distribution obtained with the BEM were less than 0.5% compared to the analytic solution (Fig. 6a).

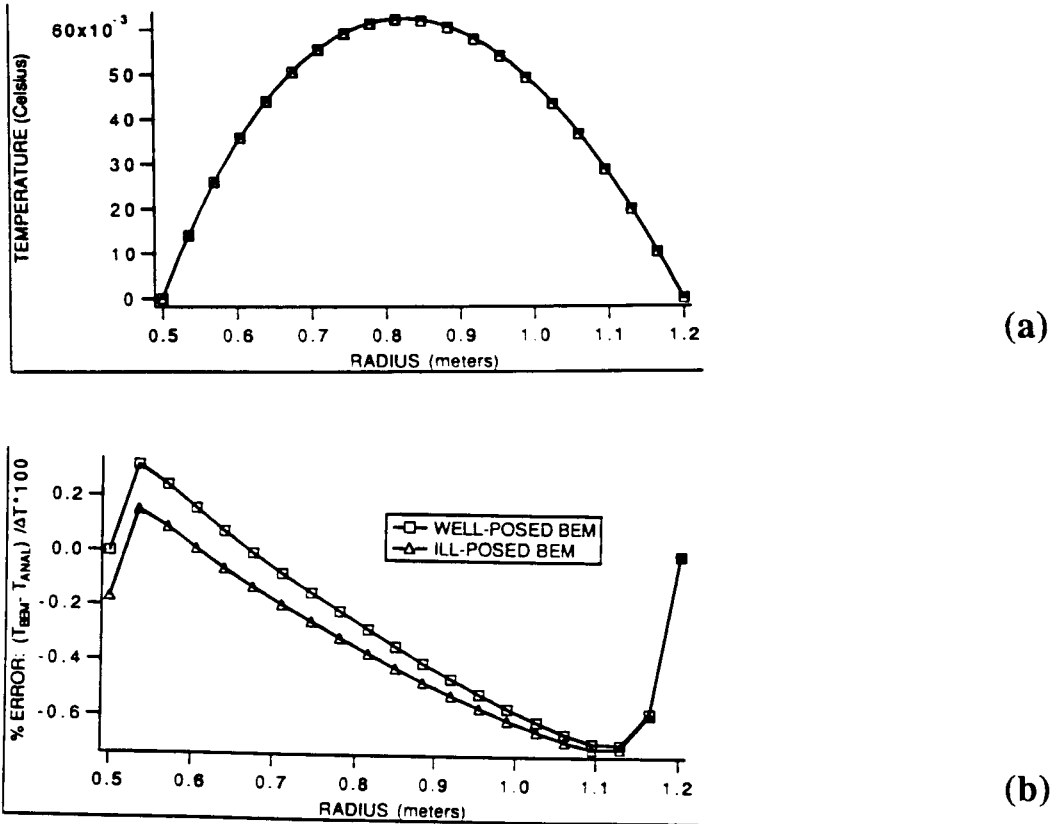


Figure 6 Results of the well-posed (squares) and inverse (triangles) BEM Poisson equation code on an annular circular disk. Radial temperature variation compared with the analytic results (a), and relative error of the well-posed BEM and the ill-posed BEM (b) when nothing was known on the inner circular boundary.

Next, the boundary conditions supplied to the BEM algorithm were changed so that they became ill-posed. The outer circular boundary was specified with $\bar{\Theta}_{\text{outer}} = 0$ and $\bar{q}_{\text{outer}} = -0.3168$ which was taken from the analytic solution. At the same time, nothing was specified on the inner circular boundary. A 72×72 BEM matrix was solved using the SVD matrix solver with a singularity threshold parameter of $\tau = 0.0001$. The BEM code in its inverse mode was successful in accurately predicting the unknown thermal boundary conditions on the inner circular boundary as well as in the entire annular domain (Fig. 6b) in a single, non-iterative run.

The algorithm was then tested against the complete analytic solution for the same geometry [8]. The analytic distribution of non-dimensional temperature was obtained within the annular domain with an arbitrary non-dimensional heat source distribution, $f(\rho, \theta)$, such that the non-dimensional temperature satisfies equation

$$\frac{\partial^2 \Theta}{\partial \rho^2} + \frac{1}{\rho} \frac{\partial \Theta}{\partial \rho} + \frac{1}{\rho^2} \frac{\partial^2 \Theta}{\partial \theta^2} + f(\rho, \theta) = 0 \quad (43)$$

With $\bar{\Theta}_{\text{outer}} = 0$ and $\bar{q}_{\text{inner}} = 0$ we can obtain an eigenfunction set written in the form of the Helmholtz equation satisfying the homogeneous boundary conditions for this configuration. After separation of variables and applying the single-valuedness condition, the analytic result for the non-dimensional temperature, Θ , is

$$\Theta(\rho, \theta) = \sum_{n=0}^{\infty} \sum_{m=1}^{\infty} R_{nm}(\rho) [A_{nm} \sin n\theta + B_{nm} \cos n\theta] \quad (44)$$

where

$$R_{nm}(\rho) = J_n\left(\mu_{nm} \frac{\rho}{\rho_{\text{inner}}}\right) - \frac{J_n\left(\mu_{nm} \frac{\rho_{\text{outer}}}{\rho_{\text{inner}}}\right)}{Y_n\left(\mu_{nm} \frac{\rho_{\text{outer}}}{\rho_{\text{inner}}}\right)} Y_n\left(\mu_{nm} \frac{\rho}{\rho_{\text{inner}}}\right) \quad (45)$$

Here, J_n and Y_n are the Bessel functions of integer order n , and μ_{nm} are the roots of the characteristic equation.

$$J_n\left(\mu_{nm} \frac{\rho_{\text{outer}}}{\rho_{\text{inner}}}\right) Y'_n(\mu_{nm}) - J'_n(\mu_{nm}) Y_n\left(\mu_{nm} \frac{\rho_{\text{outer}}}{\rho_{\text{inner}}}\right) = 0 \quad (46)$$

The Fourier coefficients, A_{nm} and B_{nm} , may be found knowing that the eigenfunctions form an orthogonal set. For example,

$$A_{nm} = \frac{\rho_{\text{inner}}^2}{\pi \mu_{nm}^2 N_{nm}} \int_{\rho_{\text{inner}}}^{\rho_{\text{outer}}} \int_0^{2\pi} \rho f(\rho, \theta) R_{nm}(\rho) \sin(n\theta) d\theta d\rho \quad (47)$$

$$B_{nm} = \frac{\rho_{\text{inner}}^2 \epsilon_n}{2 \pi \mu_{nm}^2 N_{nm}} \int_{\rho_{\text{inner}}}^{\rho_{\text{outer}}} \int_0^{2\pi} \rho f(\rho, \theta) R_{nm}(\rho) \cos(n\theta) d\theta d\rho \quad (48)$$

As a test case, we used the following expression for the heat generation term

$$f(\rho, \theta) = f_{\max} \sin \left[\frac{\rho - \rho_{\text{inner}}}{\rho_{\text{outer}} - \rho_{\text{inner}}} \pi \right] \sin \theta \quad (49)$$

For the well-posed (analysis) problem, the inner circular boundary non-dimensional temperature was specified to be $\bar{\Theta}_{\text{inner}} = 0$, the outer circular boundary was kept adiabatic, $\bar{q}_{\text{outer}} = 0$, while $f_{\max} = 1.0$. Both outer and inner boundaries were discretized with 36 linear isoparametric boundary elements and the domain was discretized with 36 x 20 quadrilateral bilinear isoparametric cells.

Thereafter, the inner boundary heat fluxes were taken from the analytic solution (Eq. (44)) and used as overspecified boundary conditions in the ill-posed (inverse) problem where nothing was specified on the outer circular boundary [8]. The comparison of the BEM solution of this analysis (or well-posed) problem (Fig. 7a) and the inverse problem (Fig. 7b) indicates an excellent agreement. The largest percentage error in computed non-dimensional temperature field is less than 0.6% and the errors in both the analysis (Fig. 7c) and inverse solution (Fig. 7d) are nearly identical.

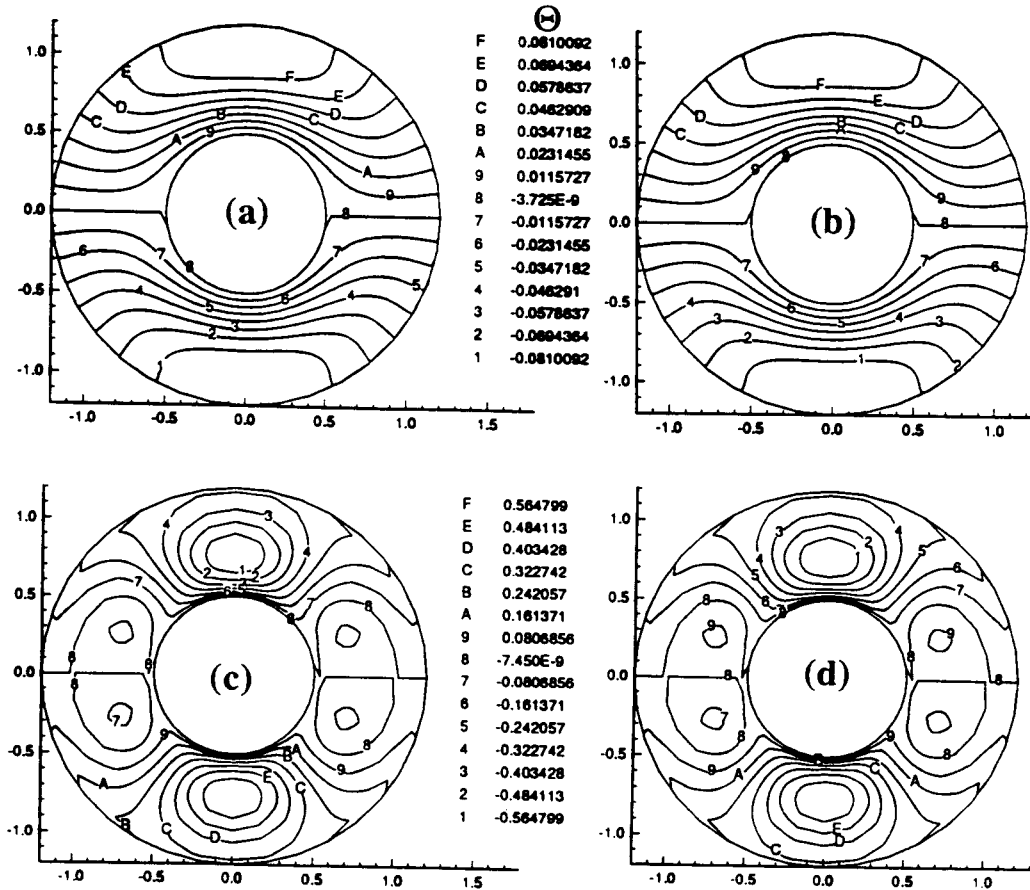


Figure 7 BEM solutions of Poisson equation on an annular circular domain with variable heat source function: a) isotherms for a well-posed problem, b) isotherms for an inverse problem when nothing was specified on the inner boundary, c) contours of constant error for a well-posed problem, and d) contours of constant error for the inverse problem when nothing was specified on the outer boundary.

3.4.8 SIHCP with internal temperature measurements. Next, given the same annular disk geometry, only the non-dimensional temperature $\bar{\Theta}_{\text{inner}} = 0$ was specified on the inner circular boundary. Heat fluxes on the inner circular boundary were treated as unknown. Non-dimensional heat source function was given as $f = 1.0$. Nothing was specified on the outer circular boundary. Instead, measurements of non-dimensional temperature were used at various locations within the domain as additional input data [8, 9]. A series of test cases were investigated for various numbers of circumferentially equidistantly spaced thermocouples set into the annular domain at $\rho = 1.0$ where the analytic value of the non-dimensional temperature is $\Theta_{\text{int}} = 0.0496$. When only four circumferentially equidistantly spaced internal non-dimensional temperature measurements were used, the resulting equation set contained 76 equations and 108 unknowns. The isotherms in Figs. 8a–8d result from using 4, 6, 9 and 18 equidistantly spaced internal temperature measurements, respectively. It can be concluded that very good results can be obtained with our SIHCP when at least 9 thermocouples are used at points within the annular domain, while only temperature is given on only one boundary [8, 9].

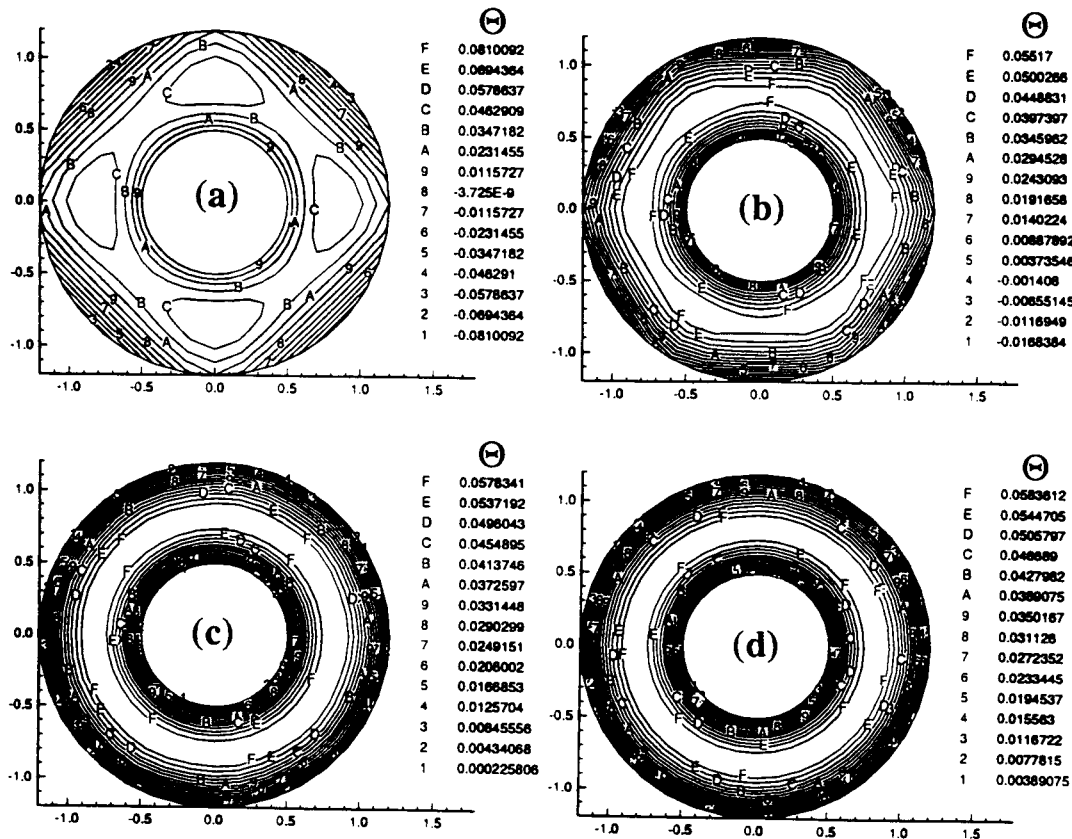


Figure 8 Isotherms predicted in an annular circular domain with a Poisson BEM code when nothing was specified on the inner circular boundary, only temperature was given on the outer boundary, and 4 (a), 6 (b), 9 (c) and 18 (d) equidistant interior measurements were provided.

3.4.9 Sensitivity to measurement errors. The major concern of researchers working on steady inverse problems is with the sensitivity of their algorithms to errors in the boundary data. In order to verify that our technique did not amplify the input data errors, normal Gaussian noise was introduced [5, 8, 9] into the non-dimensional temperature boundary condition on the outer circular boundary of the same annular region. The non-dimensional heat generation function was a constant, $f = 1.0$, and the coefficient of thermal conductivity and specimen dimensions were assumed to be accurately known. The outer circular boundary was overspecified with the flux taken from the analytic solution. Nothing was specified on the inner circular boundary. For the non-dimensional temperature boundary condition on the outer boundary, a random real number, R , between 0 and 1.0 was generated using the RANF subroutine on the CRAY-YMP computer. Using this value as the normalized probability density function, a non-dimensional temperature boundary condition was created from the following equation

$$\bar{\Theta}_{\text{outer}} = \bar{\Theta}_{\text{ave}} \pm \sqrt{-2 \sigma^2 \ln[R(\theta)]} \quad (50)$$

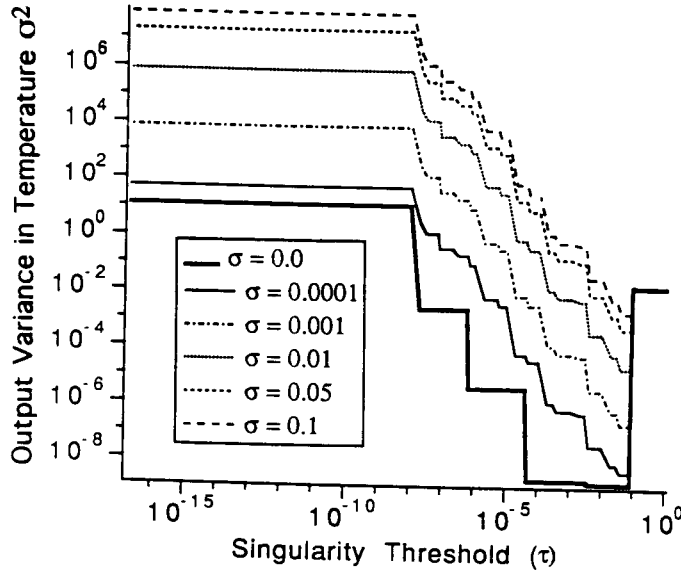
where $\bar{\Theta}_{\text{ave}}$ is the mean value taken as the non-dimensional temperature boundary condition and σ^2 is the user-specified variance of the input data. The value of $(\bar{\Theta}_{\text{ave}} = 0)$ has been chosen so that it produced a zero bias. The errors were assumed to be additive and the same variance is prescribed for all non-dimensional temperature measurements.

Our BEM program was then tested with a variety of input non-dimensional temperature standard deviations, σ , on the outer circular boundary. The resulting solution matrices were solved using the SVD algorithm and Tikhonov's regularization scheme. From the computed output variances in non-dimensional temperatures versus the range of possible τ 's and λ 's between 10^{-16} and 1.0, it can be concluded [9] that τ_{opt} does not depend (Fig. 9a) on the input σ , while λ_{opt} depends (Fig. 9b) on the input data noise. The input standard deviations, between $0 \leq \sigma \leq 0.1$, corresponding to errors from 0% up to 100% or more, yielded a minimum output variance when the singularity threshold, τ_{opt} , was $0.04 \leq \tau \leq 0.08$. The value of λ_{opt} was found by the iterative optimization process described earlier.

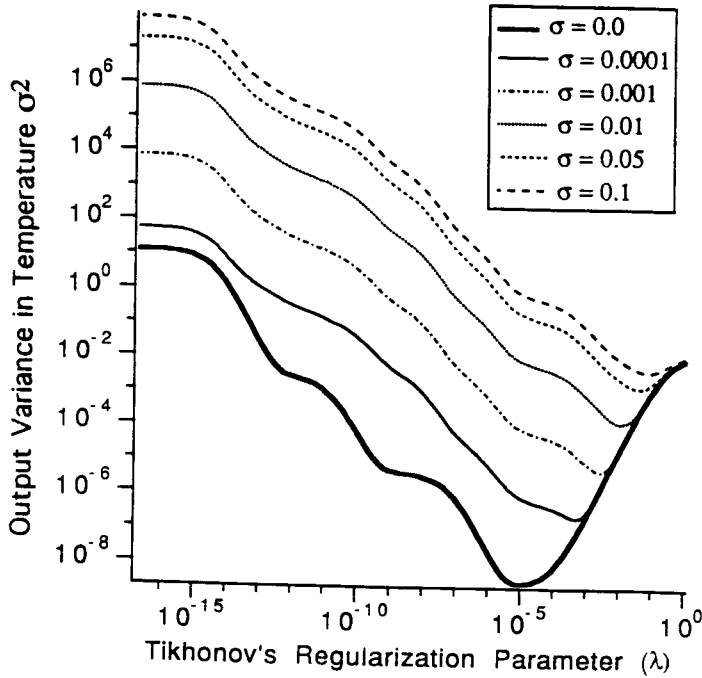
It was also found [9] that the larger values of Tikhonov's regularization parameter, λ , yielded a greater error (bias) in the global (integrated) energy conservation, although the amount of input standard deviation did not affect it directly. This implies that Tikhonov's regularization introduces artificial dissipation which affects the physics of the problem by reducing the global amount of heat transfer. Since larger λ_{opt} 's are required for higher input variances, the results obtained with Tikhonov's regularization become increasingly biased as the input measurement data becomes more noisy. On the other hand, the SVD did not exhibit this behavior. Once the threshold parameter τ was small enough, the global energy conservation became satisfied and remained unchanged for all smaller values of τ .

We conclude from these observations that the SVD technique is more robust and reliable than Tikhonov's regularization since the latter can mislead the observer into thinking that a highly biased result is correct because it appears to be smooth. With the SVD, the user will immediately recognize if the chosen value of the threshold parameter, τ , is wrong since the computed temperatures and heat fluxes will be highly oscillatory. In addition, since the correct value of integrated heat flux

is known in both well-posed and ill-posed problems, the value of τ_{opt} can be determined from this information after only 2-3 repetitive trials by starting with an initial guess $\tau < 0.1$. This is an easier procedure than with Tikhonov's method where λ_{opt} is found iteratively by simultaneously minimizing the output variance and the bias. Even with this value of λ_{opt} Tikhonov's method will create results that have a non-zero bias, while the SVD approach offers a zero bias [9].



(a)



(b)

Figure 9 Variances in the output (computed inner boundary) non-dimensional temperatures and heat fluxes as a function of the (a) SVD singularity threshold parameter, τ , and (b) Tikhonov's regularization parameter, λ , for various levels of input standard deviation, σ .

3.4.10 Temperature-dependent thermal conductivity. The ability of the BEM analysis program to predict thermal fields in materials with arbitrary temperature-dependent heat conductivity was verified in case of a rod 1.0 m long with a 0.1 m by 0.1 m cross section. The rod surface was discretised with 42 square isoparametric boundary elements each measuring 0.1 m by 0.1 m. Four sides of the rod were kept adiabatic and the remaining two opposite sides were subject to different non-dimensional temperatures ($\bar{\Theta}_{\text{hot}} = 1.0$ and $\bar{\Theta}_{\text{cold}} = 0$). The temperature-dependent thermal conductivity can be given as a polynomial function of the general type

$$k(T) = k_0 (a T^{-1} + b + cT + d T^2 + e T^3) \quad (51)$$

or, in a non-dimensional form as

$$\kappa(\Theta) = \kappa_0 (A\Theta^{-1} + B + C\Theta + D\Theta^2 + E\Theta^3) \quad (52)$$

In the case where $\kappa_0 = 1.0$, $B = 1.0$ and $A = D = E = 0$, the one-dimensional analytic solution [53] for an arbitrary value for the coefficient C is

$$\frac{C}{2}\Theta^2 + \Theta = \left(\Theta_{\text{hot}} + \frac{C}{2}\Theta_{\text{hot}}^2 \right) - \left(1 + \frac{C}{2}(\Theta_{\text{hot}} + \Theta_{\text{cold}}) \right) \frac{(z - z_{\text{hot}})}{(z_{\text{cold}} - z_{\text{hot}})} (\Theta_{\text{hot}} - \Theta_{\text{cold}}) \quad (53)$$

Figure 10 shows that the BEM results (using Kirchhoff's transformation) compared very well with the analytic solution, averaging an error of less than 0.5% for a range of values used for the parameters C .

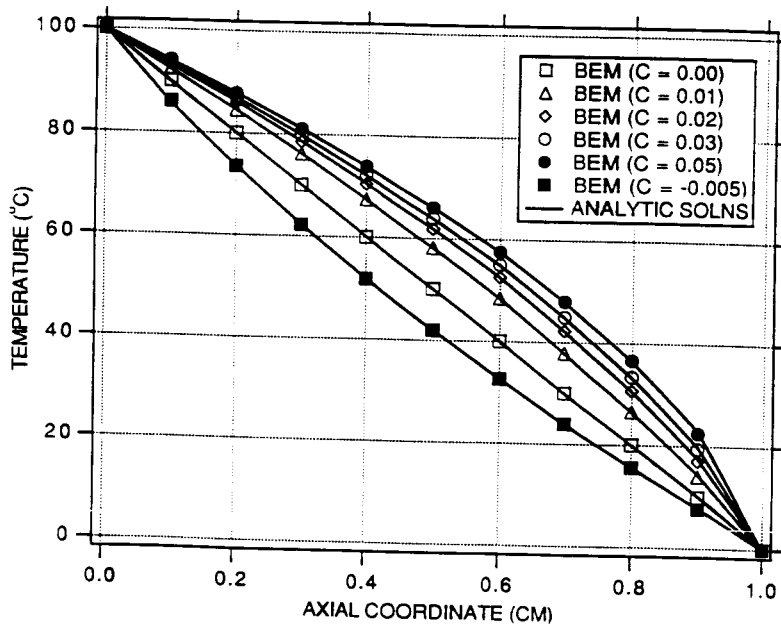


Figure 10 Comparison of analytic and BEM solutions for one-dimensional steady non-dimensional temperature distribution for different degrees of non-linearity, C , of the non-dimensional heat conductivity coefficient, $\kappa(\Theta) = \kappa_0 (1 + C\Theta)$.

4 INVERSE DETECTION OF HEAT SOURCES

The prediction of the distribution of heat sources from the measured boundary temperatures and heat fluxes can be separated into two steps. The first step is to formulate the well-posed (analysis) problem from the original statement of Fourier's heat conduction law with the application of the overspecified boundary conditions to a system of algebraic equations. The second step is the inversion of that algebraic system. The inverse problem is, by definition, ill-posed. Therefore, the solution procedure must incorporate a method which stabilizes the inversion. There are several numerical methods that have been used to solve the inverse Poisson equation. One of them, the FEM, is based on minimizing the energy function within a volume discretized into regularly shaped elements. The potential or temperature is expressed as a sum of piecewise continuous polynomial functions, called basis functions. One disadvantage of the FEM is that there can be a significant computational overhead in assembling the grid and organizing the nodes. The FDM, which is equivalent to the FEM for a regular grid, is not readily adapted to irregular geometries, but its simplicity decreases the overhead in assembling the grid. The BEM has a major advantage in that it is non-iterative and that it involves fewer nodes than does the FEM or FDM. All of the described formulations result in a set of simultaneous linear algebraic equations for the unknown internal heat sources. This matrix is highly ill-conditioned and, in general, it is not square.

As earlier mentioned, the discretized form of the set of BIE's for each boundary node can be represented in a matrix form as

$$[\tilde{\mathbf{h}}]\{\Theta\} = [\mathbf{g}]\{\mathbf{q}\} + [\mathbf{e}]\{\mathbf{f}\} \quad (54)$$

If the boundary conditions are overspecified, that is, both Θ and \mathbf{q} are known everywhere on the boundary, the vectors $\{\Theta\}$ and $\{\mathbf{q}\}$ can be multiplied by their coefficient matrices to form a vector of known quantities, $\{\mathbf{F}\}$. The system

$$[\mathbf{e}]\{\mathbf{f}\} = \{\mathbf{F}\} \quad (55)$$

can then be solved for the unknown non-dimensional heat sources, $\{\mathbf{f}\}$. The matrix $[\mathbf{e}]$ is ill-conditioned and, if internal measurement nodes are used in the formulation, it is not square. If N is the number of nodes discretizing the boundary Γ and N_{VC} is the number of nodes used to discretize the domain Ω , then there will be N equations and $N+N_{VC}$ unknowns. The matrix can be solved using either the SVD method or Tikhonov's regularization, but the accuracy of the procedure is expected to decrease with the increasing number of domain nodes and with the increasing complexity of the distribution of the heat sources.

In order to verify that the BEM is capable of finding the internal heat generation field compatible with the given overspecified boundary data, we used the

hollow circular disk geometry described earlier with $\bar{\Theta}_{outer} = \bar{\Theta}_{inner} = 0$ and $f = 1.0$. The resulting analytical values (from Eq. (42)) for the non-dimensional heat fluxes were $\bar{q}_{outer} = -0.3168$ and $\bar{q}_{inner} = 0.4296$. These fluxes were then used as the overspecified boundary conditions on the outer and inner circular boundaries in order to predict the value of the heat generation field. The accuracy of the numerical solution was determined by how the internal region was discretized. The outer and inner circular boundaries were discretized with 36 linear isoparametric elements. When the annular domain was discretized with 36 bilinear isoparametric

quadrilateral cells, having only one cell between the outer and inner circular boundaries, the results were excellent. The heat generation field was predicted with an average error less than 0.01%. Similar results were found when the heat generation was linearly varying as $f(\rho) = (\rho - \rho_{\text{inner}}) / (\rho_{\text{outer}} - \rho_{\text{inner}})$.

But, when the domain was discretized with two or more rows of bilinear isoparametric quadrilateral cells, the results were in error up to 30%. This is because the resulting assembled BEM matrix had twice as many unknowns as it had equations for the case of two rows of quadrilaterals. The highly ill-conditioned matrix could not produce good results, even when Tikhonov regularization was employed. The results were significantly improved [9] whenever internal temperature measurements were included in the analysis. For example, when the domain was discretized with two rows of quadrilateral cells, a single row of 9 known internal temperatures produced results which averaged an error of less than 0.1%. Further numerical tests have shown that whenever the temperature field is entirely known everywhere in the domain, the resulting solution matrix, $[e]$, is both square and well-conditioned (Eq. (55)). After inversion of this matrix, the unknown heat source vector $\{f\}$ can be found with an accuracy comparable to the well-posed (forward) problem, where $\{f\}$ is known and the temperature field is the objective of the computation.

5 OPTIMIZATION

The general constrained optimization problem [54, 55] can be mathematically stated as follows: minimize the cost function $F(\mathbf{x})$, where the vector of design variables is $\mathbf{x} = \{x_1, \dots, x_{n_{\text{var}}}\}$, such that $\mathbf{x}_{\text{min}} < \mathbf{x} < \mathbf{x}_{\text{max}}$ while $g_j(\mathbf{x}) \leq 0$ and $|h_j(\mathbf{x})| \leq \epsilon$. Here, \mathbf{x}_{min} is the vector of lower limit constraints, \mathbf{x}_{max} is the vector of upper limit constraints, g_j is the set of n_{icon} inequality constraint functions, h_j is the set of n_{econ} equality constraint functions, and ϵ is a very small number called the constraint thickness. There are two basic approaches to optimization; one which is based on the gradient search and the other which uses non-gradient methods.

5.1 Evolutionary Hybrid Optimization Algorithm

A constrained evolutionary hybrid optimization scheme has been developed. This algorithm creates sequential populations of feasible designs which evolve with each new optimization cycle by minimizing the cost function associated with various members of the population. There are many optimization algorithms in the open literature and various techniques have been shown to provide faster convergence over others depending upon the size and shape of the mathematical design space, the nature of the constraints and where it is during the optimization process. The hybrid algorithm incorporates three of the most popular optimization approaches: the Davidon-Fletcher-Powell (DFP) gradient search [54] method, a genetic algorithm (GA) [56], and the Nelder-Mead (NM) routine [57]. Each technique separately provides a unique approach to optimization, sometimes having good convergence and good reliability, sometimes poor convergence and good reliability, and sometimes good convergence and poor reliability.

The DFP gradient search method is generally the most expensive method but the convergence is both maximized and guaranteed. This algorithm is susceptible to local minima and can get stuck on a constraint boundary. Depending on how this procedure stalls, the optimizer switches to either the genetic algorithm or the NM routine. The DFP improves the best design in the population.

The genetic algorithm is an evolutionary approach which utilizes its random nature to escape local minima. When the average cost function of the new generation is not improved, the GA becomes an inefficient optimizer. This most often occurs when its random nature is prevalent, producing several bad and infeasible designs. The GA is then automatically switched to the NM because the NM cheaply works upon these worst designs first. When the variance in the cost function scores of the new population is very small, the population is beginning to concentrate around a possible global minimum. The optimizer is then automatically switched to the DFP because this algorithm has the ability to quickly converge on that minimum. The GA develops a new population with each iteration, saving only a few of the best or elitist designs unchanged from one iteration to the next.

The Nelder-Mead is a zeroth order method that utilizes a simplex generated by the population of previously generated designs. This algorithm is the cheapest of the three, but it does not guarantee convergence. The existing population matrix of the genetic algorithm and previously generated feasible designs from the gradient search techniques is ideal, making the NM even cheaper to employ. It improves only the worst design in the population with each iteration.

The new evolutionary hybrid scheme [58] handles the existence of constraints in three ways; Rosen's projection method, a feasible search and random design generation. Rosen's projection method provides search directions which guide it tangent to active constraint boundaries. In the feasible search, designs which violate constraints are automatically restored to feasibility via the minimization of the global constraint functions. If at any time this minimization stalls, a random design is generated within a Gaussian-shaped probability density cloud about a desirable and feasible design until a new design is reached.

The feasible set of design variables from the current optimization cycle are saved into an array called the population matrix. This population is updated every iteration with new designs and ranked according to the value of the cost function. As the optimization process proceeds, this population evolves because of the nature of the optimization process. The optimization problem is completed when the best design in the population provides a desirable target design or when the variation in the population's design characteristics becomes very small. This usually indicates that a global minimum has been found.

6 INVERSE SHAPE DESIGN

Steady state, nonlinear heat conduction can be modeled as a boundary value problem where the boundary conditions of Dirichlet, Neumann or Robin type are specified on the entire boundary of the solid object. If the thermal boundary conditions are overspecified, that is, if both the temperature and the heat flux are simultaneously enforced on the boundary or on a portion of the boundary, then the problem is overspecified and the problem is ill-posed. This means that the governing partial differential equation for the steady temperature field may not be able to satisfy simultaneously all the thermal boundary conditions. There are two possibilities to resolve this problem. One possibility is to determine the material thermal properties that can vary in a very special way from point-to-point throughout the object (the case of a thermally functional material). The other option is to find a very special distribution of the heat source function in the object as was demonstrated earlier. If the heat sources do not exist, the solution can still be found if the size and shape of the object are altered in an appropriate manner. This approach is called an inverse shape design methodology.

6.1 Inverse Shape Design Objectives

Specifically, the objective is to minimize the difference between the specified values, \bar{u}^{spec} , and the calculated values, \bar{u}^{calc} , which can be either temperature or heat flux at the overspecified boundary. The cost function, $F(\mathbf{x})$, can be mathematically formulated [17, 18] as a normalized least sum of squares

$$F(\mathbf{x}) = \frac{\sum_{j=1}^N (\bar{u}_j^{\text{spec}} - \bar{u}_j^{\text{calc}})^2}{\sum_{j=1}^N (\bar{u}_j^{\text{spec}})^2 + \epsilon} \quad (56)$$

or as a locally normalized error at each boundary element on the overspecified boundary

$$F(\mathbf{x}) = \sum_{j=1}^N \frac{(\bar{u}^{\text{spec}} - \bar{u}^{\text{calc}})_j^2}{(\bar{u}^{\text{spec}})_j^2 + \epsilon} \quad (57)$$

where \mathbf{x} is the vector of design variables. Here, ϵ is a very small user-specified parameter to avoid division by zero. The shape optimization procedure for the inverse design of internal coolant flow passages (where the outer hot surface of the internally cooled object is the overspecified boundary) then consists of the following steps:

1. Specify the shape of the outer surface of the three-dimensional object.
2. Specify the desired thermal boundary condition (either temperature or heat flux) on the outer surface of the object and on the coolant passage walls. These thermal boundary conditions will be needed to solve the well-posed boundary value problem.
3. Specify the additional thermal boundary conditions (temperature if the heat flux was already specified there or vice versa).
4. Specify manufacturing constraints such as the minimum distance between the coolant passage and the outer surface of the object.
5. Specify an initial guess for the internal cooling passage geometry. These are the design variables of the cost function and can take a variety of forms.
6. Using the BEM and the well-posed problem from step 2 above, the remaining surface thermal values are computed (if surface temperature was specified in step 2 above, then it will be surface heat flux and vice versa) at the outer or the inner boundaries. These computed surface thermal quantities certainly differ from the desired (overspecified) surface thermal values specified in step 3 above. A composite objective function is formed on the basis of a properly scaled least-squares measure of the difference between the computed and the overspecified surface thermal quantities.
7. The design variables are updated by the optimization algorithm.
8. If the optimization procedure stalls in a local minimum, the objective function is automatically switched and the optimization is continued from step 6.

During the optimization process, local minimas can occur and halt the process before achieving an optimal solution. In order to overcome such a situation, a simple technique has been devised. In this approach, whenever the optimization stalls, the formulation of the objective function is automatically switched between any one of the possible cost functions defined earlier. The new objective function

projects the problem into another function space and provides a departure from the local minima and further convergence towards the global minimum.

6.2 Design of Coolant Flow Passages

During the past several years, we have developed an inverse method that allows a thermal cooling system designer to determine the proper sizes, shapes, and locations of coolant passages (holes) in an internally cooled turbine blade [11–13, 15–20, 22–25], a scram jet strut [14], a rocket chamber wall [19, 23], etc. Using this method the designer can enforce a desired heat flux distribution on the hot outer surface of the object, while simultaneously enforcing desired temperature distributions or convective heat transfer rates on the same hot outer surface as well as on the cooled interior surfaces of each of the coolant passages. This constitutes an overspecified inverse problem which is solved by allowing the number, sizes, locations and shapes of the passages (holes) to adjust iteratively until the final internally cooled configuration satisfies the overspecified thermal boundary conditions and the governing equation for the steady temperature field. The geometry of the coolant passages make up the design variables of the cost function. Since the number of passages may also be a design variable, a problem arises when computing the gradient of the objective function. Additional holes cannot easily be added since the search should include all the possible combinations of hole location and geometry. A simple and straightforward approach is to start optimizing with a large number of holes (limited by computer memory and computational efficiency) and then reduce the number of holes during the optimization procedure. The criterion for excluding a particular hole during the optimization procedure is when the hole reduces to such a small size that it has a negligible effect on the heat flux at the outer boundary. Otherwise, the procedure is time consuming and often terminates in a local minima.

6.2.1 Minimization of number of cooling passages. Our inverse design methodology for the determination of the proper locations, shapes and sizes of a given number of coolant flow passages (holes) subject to specific surface temperatures and heat fluxes has been extended to allow the designer the freedom to guess the required number of holes and the minimal allowable diameter of a hole. A constrained optimization algorithm is then used to minimize the total number of cooling holes, while satisfying user-specified hot surface temperatures and heat fluxes. Premature termination of the optimization process due to the existence of local minimas has been satisfactorily resolved by the automatic switching of the objective function formulation whenever the local minima is detected. The convergence criteria of the iterative process, which can be specified by the user, was found to have a strong influence on the accuracy of the entire inverse design optimization algorithm.

As an example involving the application of these techniques to a realistic domain we chose a ceramically coated turbine blade airfoil (Fig. 11a) with $f = 0$, $\kappa_{\text{coating}} = 1.0$, $\kappa_{\text{metal}} = 21.0$ (where $\kappa = k/k_0$), and five circular coolant passages (holes). Then, our BEM analysis code was run with $\bar{\Theta}_{\text{inner}} = 0$ specified on the circular boundary of each hole and $\bar{\Theta}_{\text{outer}} = 1.0$ specified on the entire outer boundary of the turbine airfoil. The optimization process was then initiated by guessing that there should be ten holes (Fig. 11b) with each of them having the same $\bar{\Theta}_{\text{inner}} = 0$ while the airfoil outer boundary was assigned $\bar{\Theta}_{\text{outer}} = 1.0$. As the overspecified thermal boundary condition we iteratively enforced the heat flux

\bar{q}_{outer} that was obtained by the BEM from the well-posed problem with five holes. After 30 iterations with a constrained gradient-search DFP optimization algorithm requiring 3775 calls to the Laplace's equation integration routine, the integrated outer heat flux error reduced below 0.25%. The optimized solution (Fig. 11c) had six holes. Five of them had almost the same sizes and locations as the correct solution, while the sixth hole was still reducing to zero. This shape inverse design consumed approximately 5000 seconds on an IBM 3090 computer.

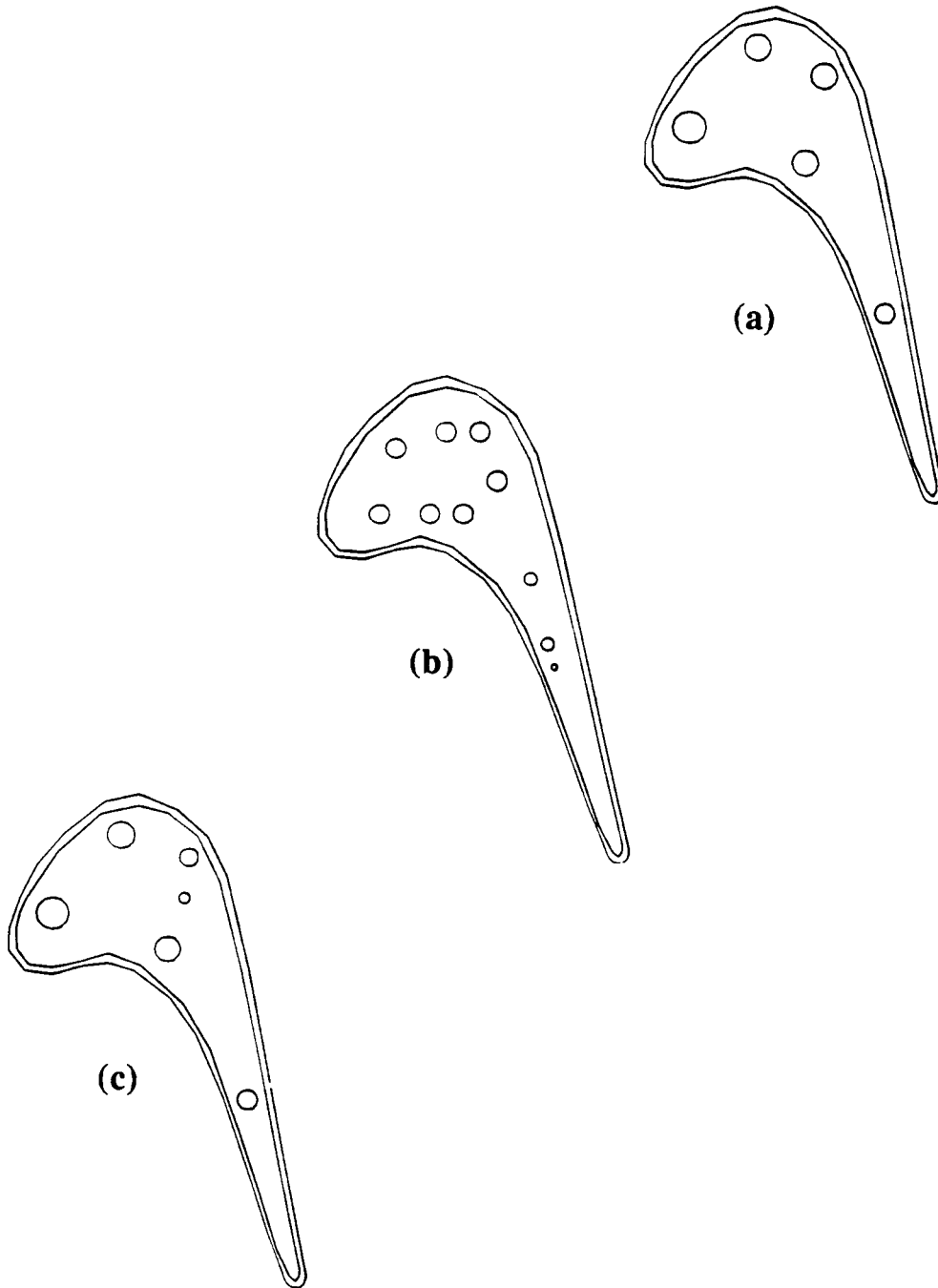


Figure 11 Minimization of the number of circular cross-section coolant passages inside a ceramically coated turbine blade airfoil: a) target geometry; b) initial guess, and c) an almost converged final result of the inverse shape design.

6.2.2 Super-elliptic holes in a coated turbine airfoil. The shapes of the holes can be arbitrary just like the shape of the outer boundary and the coating thickness distribution can be arbitrary. To demonstrate this point and the effective enforcement of the manufacturing constraints, we used [22] a realistically shaped turbine blade airfoil having a chord length of 0.083 m and the coating thickness of 0.000415 m. The thermal conductivities were $k_{\text{coating}} = 1.0 \text{ W m}^{-1} \text{ K}^{-1}$ and $k_{\text{metal}} = 23.0 \text{ W m}^{-1} \text{ K}^{-1}$. There were no heat sources, that is, $f = 0$. It was assumed that the coated airfoil has three circular interior coolant flow passages (Figs. 12a–12c and Table 2). Here, the origin of the global Cartesian coordinate system x, y is at the geometric center of the airfoil.

Table 2 Initial and converged Lamé parameters for three holes

Hole number		a (m)	b (m)	n	x_o (m)	y_o (m)	θ (deg)
1	Initial guess	0.005	0.005	2.0	-0.02	-0.0075	0.0
1	Final value	0.0075	0.005	2.0	-0.0275	-0.0025	-40.0
2	Initial guess	0.005	0.005	2.0	-0.01	-0.0075	0.0
2	Final value	0.01	0.0075	6.0	-0.0075	-0.01	0.0
3	Initial guess	0.005	0.005	2.0	0.0	-0.0075	0.0
3	Final value	0.0125	0.005	2.0	0.0275	0.01	55.0

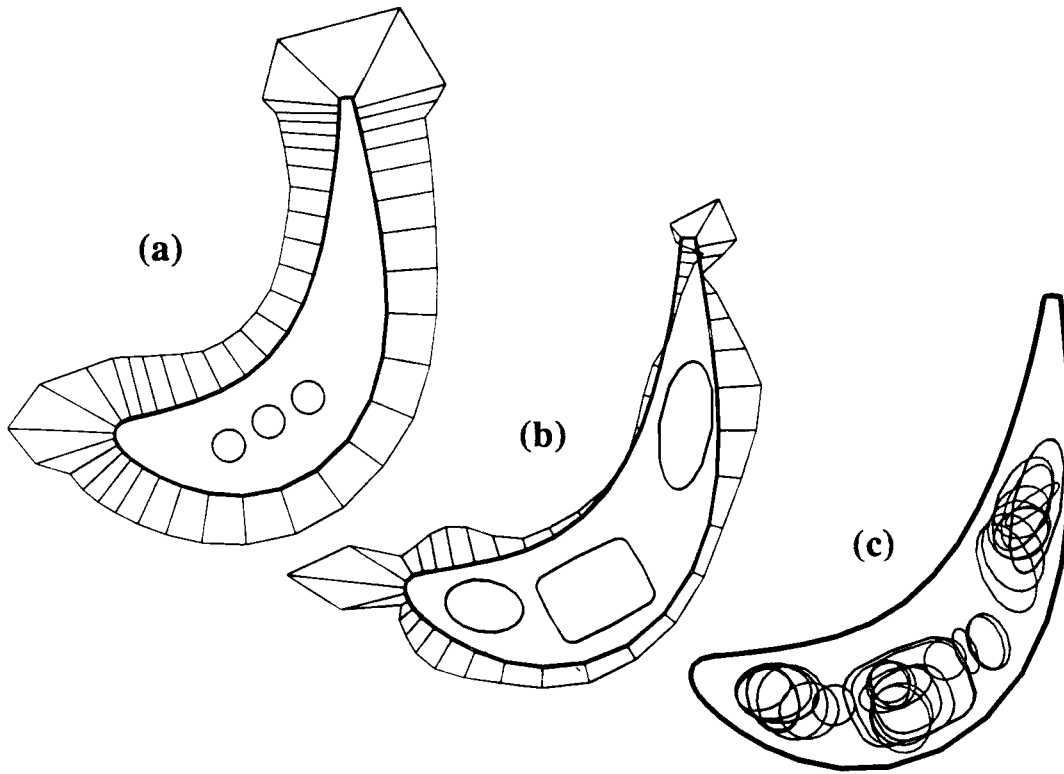


Figure 12 Inverse shape design of three coolant passages in a ceramically coated turbine blade airfoil with specified outer boundary temperatures (a) and heat fluxes (b). The iterative convergence history of the geometry of three initially circular passages (a) indicates the robustness of this procedure that utilizes a constrained optimization algorithm (b). Intermediate shapes are indicated with dashed lines (c).

All boundary conditions were of the Dirichlet type with a realistic variation of temperature specified on the airfoil outer (hot) boundary (Fig. 12a) and a constant temperature $\bar{T}_{\text{hole}} = 500.0$ K specified on the walls of each of the holes. The outer (hot) boundary of the coated airfoil was discretized with 50 linear isoparametric boundary elements. The metal/coating interface boundary was also discretized with 50 flat panels. The boundary of each of the three coolant flow passages was discretized with 20 linear isoparametric boundary elements. The boundary elements were everywhere clustered with respect to the local boundary curvature. In addition, a minimum distance of 0.0005 m between any of the holes and between any hole and the metal/coating interface were specified as the manufacturing constraints. The target heat flux is shown in Fig. 12b, while Fig. 12c depicts the geometric evolution history at several stages during the optimization process. The optimization was completed when the normalized hot boundary heat flux error (using the global cost function formulation and barrier function to incorporate the constraints) reached 1.32%. The dotted shapes (Fig. 12c) indicate the intermediate geometries and the solid shapes indicate the final solution (not fully converged) where the minimum allowable wall thickness constraint was honored. The initially circular holes transformed appropriately and moved from their initial positions to the almost correct target configuration (Fig. 12b) which would have been eventually reached by continuing the optimization process. The entire optimization in this inverse shape design case consumed 103 optimization cycles, 2859 calls to the BEM analysis routine, and 12028 seconds of CPU time on an IBM 3090 computer.

6.2.3 Super-elliptic cavity within a sphere. This test case was used to demonstrate the fully three-dimensional shape inverse design capability of the optimization algorithm with the temperature-dependent material properties. The geometry consisted of a unit sphere ($r_{\text{outer}} = 1.0$) with an off-centered cavity of a three-dimensional super-elliptic shape given by

$$\left(\frac{x' - x_o}{a} \right)^n + \left(\frac{y' - y_o}{b} \right)^n + \left(\frac{z' - z_o}{c} \right)^n = 1 \quad (58)$$

Seven design variables are derived from this equation: the center coordinates of the super-elliptic cavity (x_o, y_o, z_o), its semi-major axes (a, b, c) and the super-elliptic exponent, n . The initial shape of the cavity was given as: $x_o = 0.2$, $y_o = 0.2$, $z_o = 0.2$, $a = 0.3$, $b = 0.4$, $c = 0.5$, $n = 4.0$. The outer spherical surface and the internal super-elliptic cavity surface (Fig. 13a) were each discretized with 64 bilinear isoparametric quadrilateral panels. A constant temperature $\bar{T}_{\text{outer}} = 100.0$ K was specified on the outer boundary and $\bar{T}_{\text{inner}} = 50.0$ K on the inner super-elliptic cavity surface. The material properties were assumed such that the thermal conductivity (Eq. (51)) had $k_o = 365.6 \text{ W m}^{-1} \text{ K}^{-1}$, $a = d = e = 0$, $b = 1.0$, and $c = -0.01 \text{ K}^{-1}$. The flux specified on the outer spherical boundary was $\bar{Q}_{\text{outer}} = 59.3 \text{ K m}^{-1}$. It was taken from the BEM analysis run corresponding to the desired (target) configuration consisting of a unit sphere (having temperature-dependent thermal conductivity) with a centered spherical cavity ($r_{\text{inner}} = 0.5 \text{ m}$) subject to well-posed Dirichlet boundary conditions ($\bar{T}_{\text{outer}} = 100.0 \text{ K}$ and $\bar{T}_{\text{inner}} = 50.0 \text{ K}$). The run was terminated near the global minimum with an objective function value of 0.32% when the DFP optimization algorithm nearly reached the fully converged sphere-within-a-sphere configuration (Fig. 13b) in 50 optimization cycles. The

entire optimization procedure required 647 calls to the BEM analysis routine and consumed approximately 2235 seconds of CPU time on an IBM 3090 computer.

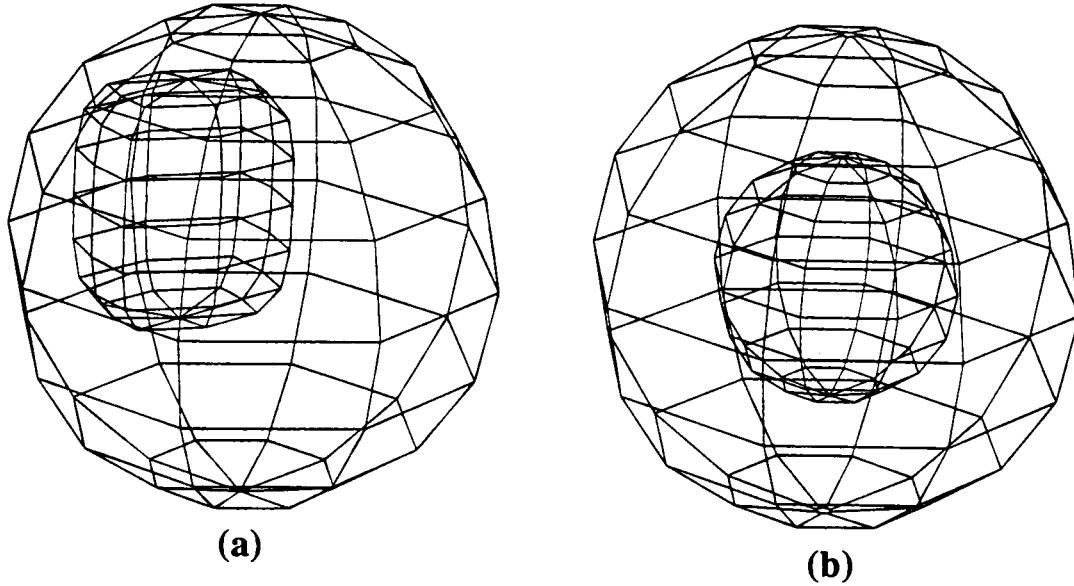


Figure 13 Demonstration of the three-dimensional inverse shape design when overspecified boundary conditions were given on the entire outer spherical boundary and nothing was specified on the inner super-elliptic off-center cavity: a) initial guess, and b) final converged answer.

6.2.4 Three-dimensional turbine blade wall thickness optimization.

This example involved the application of the inverse shape design technique to a three-dimensional turbine blade of realistic shape. The turbine blade was given a single internal coolant flow passage. The optimization objective was to determine the appropriate wall thickness inward from the specified blade's outer surface that yielded the desired overspecified thermal boundary data [24].

The surface of the three-dimensional coolant passage was generated at each radial cross section of the blade by first determining the mean airfoil thickness curve from the local blade airfoil geometry. At each blade cross section this mean thickness curve was then reduced by a fraction of its total length from the leading and trailing edges, p_{te} and p_{le} , respectively. The inner airfoil contour was then constructed by defining a wall thickness function versus the blade airfoil outer contour arc length, s . The local wall thickness, $t(s)$, was defined along a straight ray from a point on the blade airfoil outer contour to the corresponding point on the reduced mean thickness curve. The wall thickness $t(s)$ was approximated by a Chebyshev polynomial of degree n given as

$$t(s) \approx \sum_{j=1}^n c_j P_{j-1}(s) - \frac{c_1}{2} \quad (59)$$

where the Chebyshev coefficients are

$$c_j = \frac{2}{n} \sum_{k=1}^n \left[\cos\left(\frac{\pi(k-1/2)}{n}\right) \right] \cos\left(\frac{\pi(j-1)(k-1/2)}{n}\right) \quad (60)$$

and

$$P_j(s) = \cos(j \arccos s) \quad (61)$$

The polynomial of equation can be truncated to a lower degree $m \ll n$ due to the nature of the Chebyshev approximation.

The design variables that made up the coolant passage geometry consisted of m Chebyshev coefficients for each radial section of the blade in addition to the two quantities p_{te} and p_{le} , that determine by what fraction the mean thickness curve is reduced from the trailing and leading edges of each local blade airfoil. Each turbine blade section between two consecutive radial cuts was discretised with 20 clustered quadrilateral surface panels around its outer surface in addition to the same number of quadrilateral surface panels on its inner surface. There were also 20 quadrilateral panels covering the blade root cross section and 20 quadrilateral panels covering the blade tip cross section. This means that the blade wall thickness at the root and at the tip sections was discretised by single rows (Fig. 14a) of quadrilateral panels. Consequently, we used a total of 200 quadrilateral surface panels connected between 200 nodes at the panels' vertices. The desired temperature was prescribed along the outer surface of the turbine blade according to a simple formula

$$\bar{T}_{outer} = T_{min} + (T_{max} - T_{min}) [\cos(2\pi s/s_{max})]^2 \quad (62)$$

with $T_{min} = 500.0$ K and $T_{max} = 1000.0$ K at the blade root section. Each of them was increased by 50.0 K at each of the four remaining consecutive sections so that their values at the blade tip section were $T_{min} = 700.0$ K and $T_{max} = 1200.0$ K. The three-dimensional blade surface temperature field is shown in Fig. 14b.

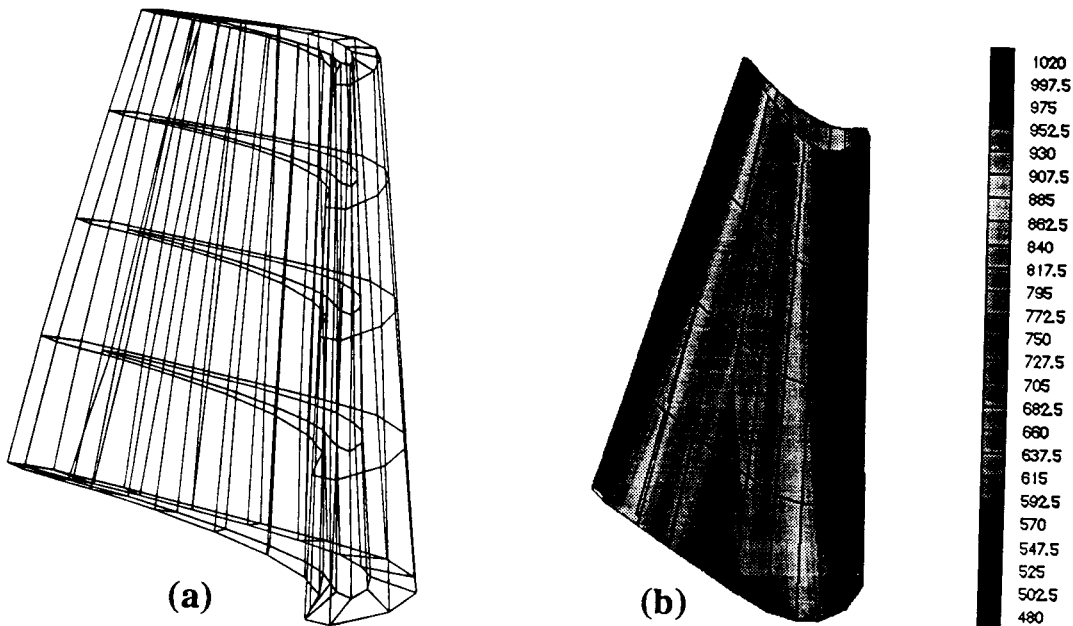


Figure 14 Computational grid (a) for the BEM on the initial guess of a three-dimensional turbine blade with a single cooling passage and specified non-uniform temperature distribution (b) on the outer surface of the blade.

In addition, a desired constant temperature was specified on the inner surface, $\bar{T}_{\text{inner}} = 300.0 \text{ K}$. The reference coefficient of thermal conductivity was $k_0 = 23.0 \text{ W m}^{-1} \text{ K}^{-1}$ and the parameters of Eq. (51) were $a = d = e = 0$, $b = 1.0$ and $c = 0.01 \text{ K}^{-1}$.

Next, a desired (target) configuration for the three-dimensional coolant passage geometry was generated. The well-posed BEM was run once with the desired temperature boundary conditions \bar{T}_{outer} and \bar{T}_{inner} . The computed outer surface non-uniform heat fluxes were then used as the overspecified boundary conditions in the shape inverse design problem where the coolant flow passage geometry was initially guessed. Figures 15a–15d illustrate the evolution of the coolant passage geometry throughout the optimization process of minimizing the least squares difference between the outer surface overspecified heat fluxes and the outer surface heat fluxes computed on the intermediate hollow blade configurations. Each figure (Figs. 15a–15d) represents a consecutive cross-section of the turbine blade showing nodes on the outer surface of the airfoil shape, the initial guess passage cross-section geometry (finely dotted line), several intermittent contours depicting the coolant target configuration (dashed lines) and the optimization process was completed after 46 iterations with the objective function reducing from an initial value of 74% to its final value of 8.64 %. The process could be resubmitted in order to further refine the coolant passage geometry. The entire optimization process required 2996 calls to the BEM analysis routine and consumed approximately 2550 seconds of CPU time on a CRAY C-90 single-processor computer.

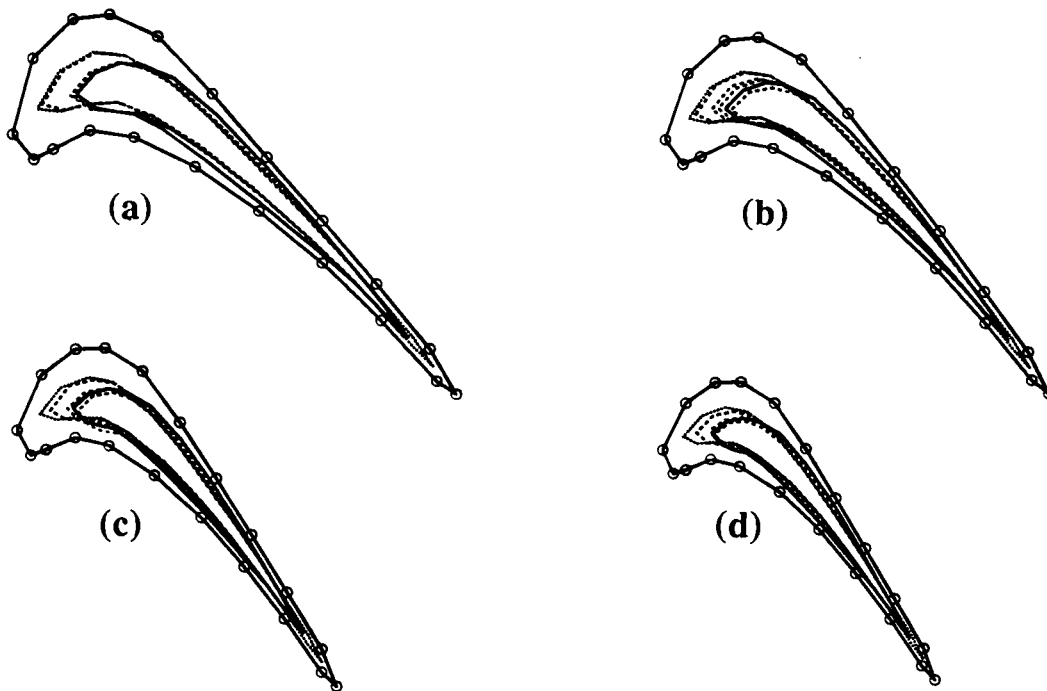


Figure 15 Geometric history of the optimization of a single coolant flow passage in a three-dimensional turbine blade showing sections at (a) $\rho = 0$, (b) $\rho = 0.25$, (c) $\rho = 0.75$, and (d) $\rho = 1.0$ subject to the specified temperatures and heat fluxes on the blade hot surface and temperatures on the coolant passage wall.

6.3 Non-Destructive Detection of Cracks and Voids

The same methodology and accompanying software have been adapted to the non-destructive detection of the number, sizes, shapes and locations of possible voids or cracks inside an arbitrarily shaped solid object [18, 19]. Assuming that the voids are free of any material and that the heat transfer inside the voids due to thermal radiation is negligible, the boundary conditions on these inner boundaries will be of the adiabatic (of the Neumann type). This methodology requires the user to provide only outer boundary thermal data that can be collected by experimentation. The BEM then uses the temperature on the outer boundary and the zero heat flux on the boundaries of the guessed voids to compute the heat flux at the outer boundary. It then compares these computed outer fluxes with the user-provided heat fluxes on the outer boundary. If they are different, then the particular configuration of cracks and voids submitted to the BEM analysis is incorrect. Then, the shapes, sizes and locations of the guessed cracks and voids are perturbed and the new corresponding heat fluxes are computed on the outer boundary. The comparison of the outer fluxes is performed again and the entire procedure repeated until the difference is satisfactorily small. The geometry perturbations of the cracks and voids is guided by an optimization algorithm.

To test the feasibility of this methodology and the optimization algorithm, a coated circular disk with a simple narrow vertical straight crack placed to the right of the center of the disk was the actual or target geometry [18, 19]. An outside

temperature boundary condition was specified as $\bar{T}_{\text{outer}} = (100.0 + 400.0 \sin\theta)$ K. Heat fluxes on the outer boundary of the disk corresponding to this internal crack were computed by the BEM and used as the overspecified boundary conditions. The initial guess geometry for the inverse problem was three vertical parallel cracks each having zero heat flux assigned on its boundaries. During the optimization, the lengths, locations of their centers, and the angles of inclination of each initially guessed crack were allowed to vary. This corresponded to four design variables per individual crack. This test case converged after 18 optimization cycles with a DFP optimizer and completed after it reduced and eliminated the two incorrectly guessed cracks. The capability of the code to detect simple thin cracks was thus verified.

7 INVERSE UNSTEADY BOUNDARY CONDITION PROBLEMS

In many problems involving unsteady cooling or heating of arbitrarily shaped objects it is often desirable to maintain a specified local cooling rate in some parts of the solid object. This can be achieved by determining the appropriate time-variation of temperature at every point of the walls of a cooling/heating container that will maintain the desired cooling rate at the desired interior points [32–36].

7.1 The Optimization Procedure

The surface temperature of the cooling container should be continuously adjusted in time and space in order to maintain the specified local prescribed cooling rates throughout the object. To implement this at every instant of time, the container wall circumferential temperature variation was approximated using a Chebyshev polynomial in terms of the scaled circumferential angle [33–35]. The coefficients of the Chebyshev polynomial were adjusted iteratively in order to maintain the desired cooling rates inside the object. The process starts by specifying an initial wall temperature distribution and deducing the corresponding Chebyshev

coefficients. These will be the initial values for the coefficients. Next, the transient temperature values are computed in the entire domain subject to the initial wall temperature distribution. From this, the local cooling rates are computed at a number of specified points inside the domain. A normalized cost function can then be formed as a sum of least squares of deviations of the computed and the specified local cooling rates. The new temperature distribution on the walls of the container is determined by minimizing the cost function at the next time step during the cooling process. Thus, the desired cooling rates are achieved throughout the object by determining the Chebyshev coefficients representing the proper variation of container wall temperatures at each instant of time.

7.2 Optimized Cryopreservation of Organs for Transplant Surgery

To demonstrate a practical application of this process, an actual canine kidney cooling was approximated by three nested two-dimensional regions (Fig. 16). The outer circular boundary represented the wall of a cooling container filled with a cryopreservation gelatin thus eliminating a possibility of heat transfer by convection. The two inner regions simulated the two distinct tissues of a kidney. Each of the three subdomains had a different thermal diffusivity ($\alpha_1 = 0.00154 \text{ m}^2 \text{ s}^{-1}$, $\alpha_2 = 0.0169 \text{ m}^2 \text{ s}^{-1}$, $\alpha_3 = 0.0255 \text{ m}^2 \text{ s}^{-1}$). The entire domain was discretized using 418 triangular isoparametric linear elements (Fig. 16) and 114 boundary nodes.

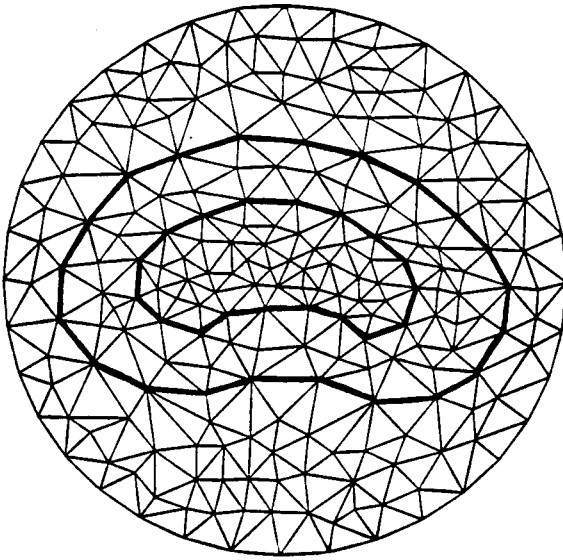


Figure 16 A triangular BEM grid for a three-domain model of a kidney in a cylindrical cooler container.

The initial temperature of the configuration was uniform ($T_{\text{initial}} = 305.0 \text{ K}$). Although each type of tissue had considerably different thermal properties and optimal cooling rates, the desired cooling rate was specified to be $\partial T / \partial t = -2.5 \text{ K min}^{-1}$ within every triangular element forming the domain approximating the two types of kidney tissue. No cooling rate was prescribed in the cryopreservation

gelatin. A sixth order Chebyshev polynomial [33, 34] in terms of the circumferential angle was used to represent the variable boundary temperature on the boundary of the container. Instead of the Chebyshev polynomial one could use a Bezier polynomial or a β -spline. Due to the low diffusivity of the cryopreservation gelatin, the cooling rate was not optimized during the first 5 minutes of the problem. The relative average error of the cooling rate with the initial container wall temperature kept fixed at $\bar{T}_{\text{wall}} = 80.0$ K was 11.7% after 10 minutes. In contrast, with optimization of the container wall temperatures performed after every 30 seconds the relative error of the cooling rate was equal to 0.26%. The relative local cooling rate errors after 15 and 20 minutes were consistently held to less than 1% when optimization was continuously used every 30 seconds. Circumferential variation of optimized container wall heat fluxes (Fig. 17a) and temperatures (Fig. 17b) indicates the potential of this method and the feasibility of the enforcement of optimized local cooling rates.

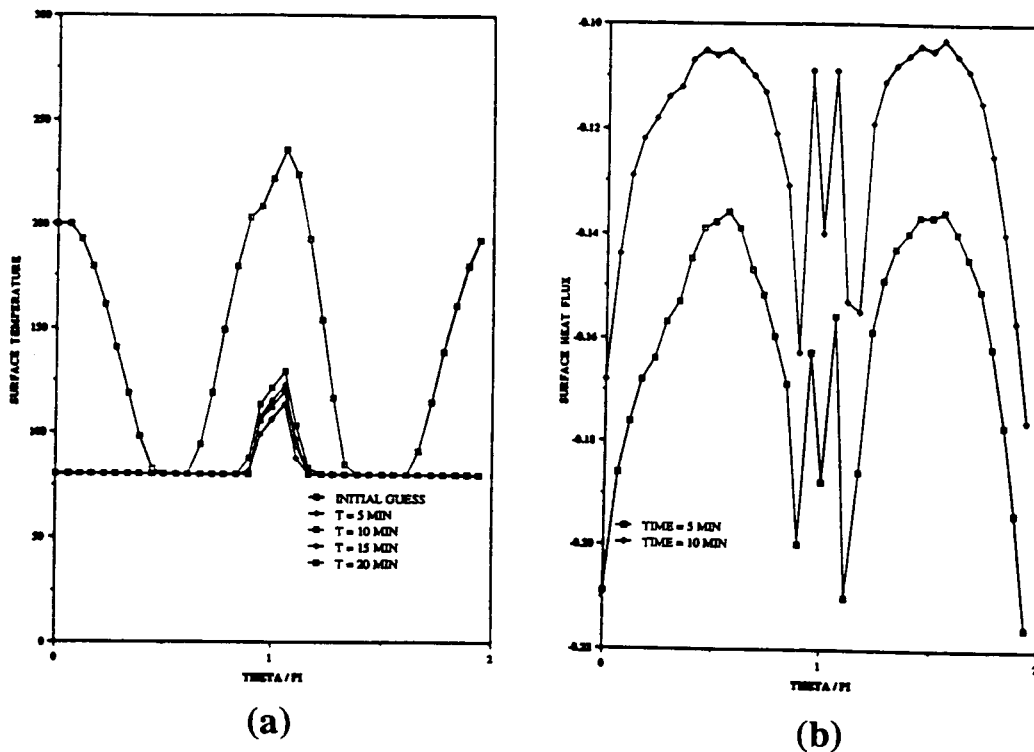


Figure 17 Optimized circumferential distribution of temperatures (a) and heat fluxes (b) on the cylindrical wall of the cooler at different times during the freezing process with the objective of maintaining the specified local cooling rate throughout the kidney at each instant of time.

8 RECOMMENDATIONS FOR FUTURE RESEARCH

We have demonstrated a number of concepts for achieving a solution of seemingly unsolvable (ill-posed) problems in heat conduction. We have utilized the BEM because of its unique abilities to propagate the information from the boundaries throughout the domain without the need for iterations. Consequently, the presented methodologies are computationally efficient and robust. However, further improvements in computational efficiency are possible especially in the field of

constrained optimization algorithms. Similarly, further improvements in the computational efficiency and especially in reliability are warranted for the SVD type matrix solution algorithms dealing with highly singular matrices.

It should be plausible to understand how optimization can be effectively used to determine the coefficients of an arbitrary polynomial (Eq. (51)) describing the unknown temperature-dependent heat conductivity of the solid material. This opens up the possibility of determining the proper spatial variation of thermal conductivity that will satisfy the desired overspecified thermal boundary conditions on the object of a given size and shape. The method of inverse determination of unknown thermal boundary conditions can easily be applied to objects composed of subdomains made of different materials. If each of these subdomains has a different temperature-dependent heat conductivity, our inverse method will become iterative. Shape inverse design could be performed considerably more efficiently if a hybrid optimization algorithm consisting of a gradient search and a non-gradient search method is used [58]. An even more efficient method might be the use of sensitivity analysis or an adjoint operator formulation [26]. In the case of unsteady cooling or warming involving phase change it should be possible to incorporate the latent heat effects via an apparent heat capacity while determining unsteady wall temperatures that will produce local desired freezing or thawing rates.

Finally, these BEM algorithms for the solution of inverse problems in linear and non-linear heat conduction can be modified and applied to inverse problems in elasticity [59], fluid mechanics [60], electromagnetism [50] and other field theories.

9 REFERENCES

1. S. Kubo, Classification of Inverse Problems Arising in Field Problems and Their Treatments, in *Proceedings of 1st IUTAM Symposium on Inverse Problems in Engineering Mechanics* (ed. M. Tanaka and H.D. Bui), Tokyo, May 11–16, 1992, Springer-Verlag, Berlin, pp. 51–60, 1993.
2. T.J. Martin and G.S. Dulikravich, A Direct Approach to Finding Unknown Boundary Conditions in Steady Heat Conduction, in *Proc. of 5th Annual Thermal and Fluids Workshop*, NASA CP-10122, Lewis Research Center, Ohio, August 16–20, 1993, pp. 137–149, 1993.
3. T.J. Martin and G.S. Dulikravich, Inverse Determination of Temperatures and Heat Fluxes on Inaccessible Surfaces, *Boundary Element Technology IX*, Computational Mechanics Publications, Southampton (ed. C.A. Brebbia and A. Kassab), pp. 69–76, 1994.
4. T.J. Martin and G.S. Dulikravich, Finding Unknown Surface Temperatures and Heat Fluxes in Steady Heat Conduction, in *Proceedings of 4th Intersociety Conference on Thermal Phenomena in Electronic Systems* (ed. A. Ortega and D. Agonafer), Washington, D. C., May 4–7, 1994, pp. 214–221; also in *IEEE Transactions of Components, Packaging and Manufacturing Technology (CPMT) Society –Series A*, Vol. 18, No. 3, pp. 540–545, September 1995.
5. G.S. Dulikravich and T.J. Martin, Inverse Problems and Design in Heat Conduction, in *Proceedings of 2nd IUTAM International Symposium on Inverse Problems in Engineering Mechanics* (ed. H.D. Bui, M. Tanaka, M. Bonnet, H. Maigre, E. Luzzato, and M. Reynier), Paris, France, November 2–4, 1994, A. A. Balkema, Rotterdam, pp. 13–20, 1994.
6. T.J. Martin and G.S. Dulikravich, Finding Temperatures and Heat Fluxes on Inaccessible Surfaces in 3-D Coated Rocket Nozzles, in *Proceedings of 1995*

- JANNAF (Joint Army-Navy-NASA-Air Force) Propulsion and Subcommittee Joint Meeting*, Tampa, FL, December 4-8, 1995.
7. Y. Kagawa, Y.-H. Sun, and O. Matsumoto, Inverse Solution of Poisson Equation Using DRM Boundary Element Model - Identification of Space Charge Distribution, *Inverse Problems in Engineering*, Vol. 1, No. 3, pp. 247-266, 1995.
 8. T.J. Martin and G.S. Dulikravich, Inverse Determination of Boundary Conditions in Steady Heat Conduction With Heat Generation, in *Symposiums on Conjugate Heat Transfer, Inverse Problems, and Optimization, and Inverse Problems in Heat Transfer* (ed. W.J. Bryan and J.V. Beck), ASME National Heat Transfer Conference, Portland, OR, August 6-8, 1995, ASME HTD-Vol. 312, pp. 39-46, 1995.
 9. T.J. Martin and G.S. Dulikravich, Inverse Determination of Boundary Conditions and Sources in Steady Heat Conduction With Heat Generation, to appear in *ASME Journal of Heat Transfer*, 1996.
 10. C.K. Hsieh and K.C. Su, A Methodology of Predicting Cavity Geometry Based on the Scanned Surface Temperature Data - Prescribed Surface Temperature at the Cavity Side, *ASME Journal of Heat Transfer*, Vol. 102, pp. 324-329, May 1980.
 11. S.R. Kennon and G.S. Dulikravich, The Inverse Design of Internally Cooled Turbine Blades, *ASME Journal of Engineering for Gas Turbines and Power*, Vol. 107, pp. 123-126, January 1985.
 12. S.R. Kennon and G.S. Dulikravich, Inverse Design of Multiholed Internally Cooled Turbine Blades, *International Journal of Numerical Methods in Engineering*, Vol. 22, No. 2, pp. 363-375, 1986.
 13. S.R. Kennon and G.S. Dulikravich, Inverse Design of Coolant Flow Passages Shapes With Partially Fixed Internal Geometries, *International Journal of Turbo & Jet Engines*, Vol. 3, No. 1, pp. 13-20, 1986.
 14. G.S. Dulikravich, T.L. Chiang, and L.J. Hayes, Inverse Design of Coolant Flow Passages in Ceramically Coated Scram-Jet Combustor Struts, ASME WAM'86, Anaheim, CA, December 1986, in *Proceedings of Symposium on Numerical Methods in Heat Transfer* (ed. M. Chen and K. Vafai), ASME HTD-Vol. 62, pp. 1-6, 1986.
 15. T.L. Chiang and G.S. Dulikravich, Inverse Design of Composite Turbine Blade Circular Coolant Flow Passages, *ASME Journal of Turbomachinery*, Vol. 108, pp. 275-282, Oct. 1986.
 16. G.S. Dulikravich, Inverse Design and Active Control Concepts in Strong Unsteady Heat Conduction, *Applied Mechanics Reviews*, Vol. 41, No. 6, pp. 270-277, June 1988.
 17. G.S. Dulikravich and B. Kosovic, Minimization of the Number of Cooling Holes in Internally Cooled Turbine Blades, *ASME paper 91-GT-103*, ASME Gas Turbine Conf., Orlando, Florida, June 2-6, 1991; also in *Internat. Journal of Turbo & Jet Engines*, Vol. 9, No. 4, pp. 277-283, 1992.
 18. G.S. Dulikravich, Inverse Design of Proper Number, Shapes, Sizes and Locations of Coolant Flow Passages, in *Proceedings of the 10th Annual CFD Workshop* (ed. R. Williams), NASA MSFC, Huntsville, AL, April 28-30, 1992, NASA CP-3163, Part 1, pp. 467-486, 1992.
 19. G.S. Dulikravich and T.J. Martin, Determination of Void Shapes, Sizes and Locations Inside an Object With Known Surface Temperatures and Heat Fluxes, in *Proceedings of the IUTAM Symposium on Inverse Problems in*

- Engineering Mechanics* (ed. M. Tanaka and H.D. Bui), Tokyo, Japan, May 11–15, 1992; also in Springer-Verlag, pp. 489–496, 1993.
20. G.S. Dulikravich and T.J. Martin, Determination of the Proper Number, Locations, Sizes and Shapes of Superelliptic Coolant Flow Passages in Turbine Blades, in *Proceedings of the International Symposium on Heat and Mass Transfer in Turbomachinery (ICHMT)* (ed. R.J. Goldstein, A. Leontiev, and D. Metzger), Athens, Greece, August 24–28, 1992.
 21. T. Matsumoto, M. Tanaka, and H. Hirata, Optimal Design of Cooling Lines of Injection Mold Based on Boundary Element Design Sensitivity Analysis, in *Inverse Problems in Engineering Mechanics* (ed. M. Tanaka and H.D. Bui), Springer-Verlag, Berlin, pp. 243–252, 1993.
 22. G.S. Dulikravich and T.J. Martin, Design of Proper Super-Elliptic Coolant Passages in Coated Turbine Blades With Specified Temperatures and Heat Fluxes, AIAA paper 92–4714, *4th AIAA/AHS/ASME Symposium on Multidisciplinary Analysis & Optimization*, Cleveland, Ohio, Sept. 21–23, 1992; also in *AIAA Journal of Thermophysics and Heat Transfer*, Vol. 8, No. 2, pp. 288–294, April – June 1994.
 23. T.J. Martin and G.S. Dulikravich, Inverse Design of Threedimensional Shapes With Overspecified Thermal Boundary Conditions, *Inverse Problems in Mechanics* (ed. S. Kubo), Atlanta Technology Publications, Atlanta, GA, pp. 128–140, September 1993.
 24. G.S. Dulikravich and T.J. Martin, Three-Dimensional Coolant Passage Design for Specified Temperatures and Heat Fluxes, AIAA paper 94–0348, AIAA Aerospace Sciences Meeting, Reno, NV, January 10–13, 1994.
 25. G.S. Dulikravich and T.J. Martin, Geometrical Inverse Problems in Three-Dimensional Non-Linear Steady Heat Conduction, *Engineering Analysis with Boundary Elements*, Vol. 15, pp. 161–169, 1995.
 26. R.A. Meric, Differential and Integral Sensitivity Formulations and Shape Optimization by BEM, *Engineering Analysis with Boundary Elements*, Vol. 15, pp. 181–188, 1995.
 27. G. Stolz, Numerical Solutions to an Inverse Problem of Heat Conduction for Simple Shapes, *ASME J. of Heat Transfer*, Vol. 82, pp. 20–26, 1960.
 28. E.M. Sparrow, A. Haji-Sheikh, and T.S. Lundgren, The Inverse Problem in Transient Heat Conduction, *Journal of Applied Mechanics, Transactions of ASME, Series E*, Vol. 86, pp. 369–375, 1964.
 29. J.V. Beck, B. Blackwell, and C.R. St. Clair, *Inverse Heat Conduction: Ill-Posed Problems*, Wiley-Interscience, New York, 1985.
 30. B. Dorri, Inverse Heat Conduction Analysis Using Boundary Integral and Finite Element Formulations, AIAA/ASME Thermophys. and Heat Transfer Conference, June 18–20, 1990, Seattle, WA, in *Symposium on Numerical Heat Transfer* (ed. K. Vafai and J.L.S. Chen), ASME HTD–Vol. 130, pp. 87–93, 1990.
 31. T.R. Hsu, N.S. Sun, G.G. Chen, and Z.L. Gong, Finite Element Formulation for Two-Dimensional Inverse Heat Conduction Analysis, *ASME Journal of Heat Transfer*, Vol. 114, pp. 553–557, 1992.
 32. L.J. Hayes, G.S. Dulikravich, and T.L. Chiang, Inverse Design and Optimization of the Cryopreservation Procedures, in *Proc. of 2nd ASME-JSME Thermal Eng. Joint Conf.*, Honolulu, Hawaii, March 22–27, 1987.
 33. J.V. Madison, G.S. Dulikravich, and L.J. Hayes, Optimization of Container Wall Temperature Variation During Transplant Tissue Cooling, in *Proceedings of International Conference on Inverse Design Concepts and*

- Optimization in Engineering Sciences (ICIDES-II)*, The Pennsylvania State University, University Park, PA, Oct. 26–28, 1987.
34. G.S. Dulikravich and L.J. Hayes, Control of Surface Temperatures to Optimize Survival in Cryopreservation, ASME Winter Annual Meeting, Chicago, Illinois, Nov. 27 - Dec. 2, 1988, in *Proceedings of the Symposium on Computational Methods in Bioengineering* (ed. R.L. Spilker and B.R. Simon), ASME BED–Vol.9, pp. 255–265, 1988.
 35. G.S. Dulikravich, J.V. Madison, and L.J. Hayes, Control of Interior Cooling Rates in Heterogeneous Materials by Varying, Surface Thermal Boundary Conditions, in *Proceedings of 1st Pan-American Congress of Applied Mechanics (PACAM-II)* (ed. C.R. Steele and L. Bevilacqua), Rio de Janeiro, Brazil, January 3–6, 1989, pp. 420–423, 1989.
 36. C. Ambrose, L.J. Hayes, and G.S. Dulikravich, An Active Control System for Thermal Fields in Hypothermic Processes, in *Proc. of National Heat Transfer Conf.*, Philadelphia, PA, Aug. 6–9, 1989 (ed. S.B. Yilmaz), AIChE Symposium Series 269, Vol. 85, pp. 440–405, 1989.
 37. A.N. Tikhonov and V.Y. Arsenin, *Solutions of Ill-Posed Problems*, New York, John Wiley & Sons, Chap. II–V, 1977.
 38. D.A. Murio, *The Mollification Method and the Numerical Solution of Ill-Posed Problems*, John Wiley & Sons, Inc., New York, 1993.
 39. G.H. Golub and C. Reinsch, Singular Value Decomposition and Least Squares Solutions, *Numerical Mathematics* (Handbook Series Linear Algebra), Vol. 14, pp. 403–420, 1970.
 40. *Proceedings of the 1st International Conference on Inverse Design Concepts in Engineering Sciences (ICIDES-I)* (ed. G.S. Dulikravich), University of Texas, Department of Aerospace Engineering & Engineering Mechanics, Austin, TX, October 17–19, 1984.
 41. *Proceedings of the 2nd International Conference on Inverse Design Concepts and Optimization in Engineering Sciences (ICIDES-II)* (ed. G.S. Dulikravich), The Pennsylvania State University, University Park, PA, October 26–28, 1987.
 42. *Proceedings of the 3rd International Conference on Inverse Design Concepts and Optimization in Engineering Sciences (ICIDES-III)* (ed. G.S. Dulikravich), Washington, D.C., October 23–25, 1991.
 43. C.A. Brebbia, *The Boundary Element Method for Engineers*, John Wiley & Sons, New York, 1978.
 44. C.A. Brebbia and J. Dominguez, *Boundary Elements, An Introductory Course*, McGraw-Hill Book Company, New York, 1989.
 45. J.C.F. Telles, A Self-Adaptive Co-Ordinate Transformation for Efficient Numerical Evaluation of General Boundary Element Integrals, *International Journal for Numerical Methods in Eng.*, Vol. 24, pp. 959–973, 1987.
 46. *International Mathematical and Statistical Libraries*, Reference Manual, edition 9, revised June 1982.
 47. Y. Rudy and B.J. Messinger-Rapport, The Inverse Problem in Electro-Cardiography: Solutions in Terms of Epicardial Potentials, *CRC Critical Reviews in Biomedical Engineering*, Vol. 16, pp. 215–268, 1988.
 48. R.D. Throne and L.G. Olson, A Generalized Eigensystem Approach to the Inverse Problem of Electrocardiography, *IEEE Transactions on Biomedical Engineering*, Vol. 41, no. 6, pp. 1–9, 1994.
 49. W.H. Press, S.A. Teukolsky, W.T. Vetterling, and B.P. Flannery, *Numerical Recipes in FORTRAN: The Art of Scientific Computing*, Second Edition, Cambridge University Press, 1992.

50. K. Pawluk, *Computational Magnetism*, Chapter 5 (ed. J.K. Sykulski), Chapman & Hall, London, 1995.
51. A.J. Kassab and R.S. Nordlund, Addressing the Corner Problem in BEM Solution of Heat Conduction Problems, *Communications in Numerical Methods in Engineering*, Vol. 10, pp. 385–392, 1994.
52. R.J. Quentmeyer, An Experimental Investigation of High-Aspect-Ratio Cooling Passages, NASA TM–105679, 1992.
53. A.J. Chapman, *Heat Transfer*, McMillan Co., New York, 1960.
54. G.N. Vanderplaats, *Numerical Optimization Techniques for Engineering Design*, McGraw-Hill, New York, 1984.
55. K.A. Haftka and Z. Gurdal, *Elements of Structural Optimization*, 3rd ed., Kluwer Academic Publishers, Boston, MA, 1992.
56. D.E. Goldberg, *Genetic Algorithms in Search, Optimization and Machine Learning*, Addison-Wesley, 1989.
57. J.A. Nelder and R. Mead, A Simplex Method for Function Minimization, *Computer Journal*, Vol. 7, pp. 308–313, 1965.
58. N.F. Foster, G.S. Dulikravich, and J. Bowles, Three-Dimensional Aerodynamic Shape Optimization Using Genetic Evolution and Gradient Search Algorithms, AIAA paper 96-0555, Reno, NV, January 15–18, 1996.
59. T.J. Martin, J.D. Halderman, and G.S. Dulikravich, An Inverse Method for Finding Unknown Surface Traction and Deformations in Elastostatics, in *Symposium on Inverse Problems in Mechanics*, ASME WAM'94 (ed. S. Saigal and L.G. Olson), Chicago, IL, November 6–11, 1994, ASME AMD–Vol. 186, pp. 57–66; also in *Computers and Structures*, Vol. 56, No. 5, Sept. 1995, pp. 825–836.
60. G.S. Dulikravich, Shape Inverse Design and Optimization for Three-Dimensional Aerodynamics, AIAA invited paper 95-0695, AIAA Aerospace Sci. Meeting, Reno, NV, Jan. 9–12, 1995; to appear in *AIAA J. of Aircraft*.